Results in Engineering 21 (2024) 102002

Contents lists available at ScienceDirect

Results in Engineering

journal homepage: www.sciencedirect.com/journal/results-in-engineering

Combining artificial intelligence and computational fluid dynamics for optimal design of laterally perforated finned heat sinks

Seyyed Amirreza Abdollahi [a], Ali Basem [b], As'ad Alizadeh [c], Dheyaa J. Jasim [d], Mohsen Ahmed [e], Abbas J. Sultan [f,g], Seyyed Faramarz Ranjbar [a], Hamid Maleki [h,*]

[a] Faculty of Mechanical Engineering, University of Tabriz, Tabriz, Iran
[b] Faculty of Engineering, Warith Al-Anbiyaa University, Karbala 56001, Iraq
[c] Department of Civil Engineering, College of Engineering, Cihan University-Erbil, Erbil, Iraq
[d] Department of Petroleum Engineering, Al-Amarah University College, Maysan, Iraq
[e] Imam Abdulrahman Bin Faisal University, P.O. Box 1982, Dammam, 31441, Eastern Province, Kingdom of Saudi Arabia
[f] Department of Chemical Engineering, University of Technology- Iraq, Baghdad, Iraq
[g] Department of Chemical and Biochemical Engineering, Missouri University of Science and Technology, Rolla, MO 65409-1230, USA
[h] Department of Mechanical Engineering, Isfahan University of Technology, Isfahan, Iran

ARTICLE INFO

Keywords:
Heat sink
CFD
Artificial intelligence
NSGA-II algorithm
MCDM

ABSTRACT

The efficient design of heat sinks is a severe challenge in thermo-fluid engineering. A creative and innovative way is applying lateral perforations to parallel finned heat sinks. The significance of achieving an optimal design for perforated finned heat sinks (PFHSs) has inspired the present authors to introduce a novel hybrid designing approach that combines computational fluid dynamics (CFD), machine learning (ML), multi-objective optimization (MOO), and multi-criteria decision-making (MCDM). The design variables considered include the size ($0.25<\varphi<0.5$) and shape (square, circular, and hexagonal) of the perforations, as well as the airflow Reynolds number ($2000<Re<5000$). The design objectives have been redefined as dimensionless parameters to assess heat dissipation, pressure drop, and heat sink weight. These modified objectives encompass thermal performance (TP), thermo-hydraulic performance (THP), and thermo-volumetric performance (TVP). The modeling process showed that both stepwise mixed selection (SMS) and GMDH-NN techniques exhibited comparable performance in most modeling scenarios. Nevertheless, the SMS approach demonstrated more reliability in modeling diverse objectives. Furthermore, the optimization results demonstrated that the optimal size of the perforations is strongly dependent on their shapes. In PFHSs with square perforations, approximately 54% of the Pareto points had a φ-value greater than 0.45. Meanwhile, in PFHSs based on circular perforations, more than 50% of the optimal points have φ less than 0.4. The MCDM-based analysis on various real-world scenarios indicated that using PFHSs with square-shaped perforations with Reynolds numbers around 2000 and considering a wide range of perforations' sizes could result in optimal designs.

1. Introduction

In recent years, the advancement of heat transfer equipment has encountered various challenges, specifically in improving productivity and thermal efficiency while concurrently reducing energy consumption and size. These ideals can be accomplished by implementing heat transfer enhancement methods (HTEMs) [1,2]. HTEMs offer promising solutions to overcome obstacles and achieve the desired objectives in heat transfer technology. HTEMs fall into two categories: active and passive. The active type uses external power such as electric fields [3], magnetic fields [4], fans/pumps [5], jets [6], and fluid/surface vibration [7,8]. In contrast, the passive type adds items such as porous materials [9], micro/nano-sized materials [10–16], ribs [17,18], vortex generators [19], and twisted tapes [20] to the system. Furthermore, passive techniques include geometric corrections such as surface roughness [21,22] and extended surfaces [23–25]. Extended surfaces or fins have significant potential to boost the heat transfer rate between the surface and the surrounding environment, making them a viable option in many real-world applications [26]. Fins can be used in radial [27], annular [28], rectangular [29], and pin-shaped [30] types according to the

* Corresponding author.
E-mail address: hamid_maleki_2010@yahoo.com (H. Maleki).

https://doi.org/10.1016/j.rineng.2024.102002
Received 2 November 2023; Received in revised form 21 January 2024; Accepted 8 March 2024
Available online 11 March 2024
2590-1230/© 2024 The Authors. Published by Elsevier B.V. This is an open access article under the CC BY license (http://creativecommons.org/licenses/by/4.0/).

primary heat transfer surface.

Rectangular fins have gained significant practical applications due to their favorable hydrothermal performance, ease of production, and compatibility with different base surfaces [31]. These factors have prompted researchers to extensively investigate and assess the utilization of rectangular fins in various analytical, experimental, and numerical studies [32]. Adhikari et al. [33] conducted comprehensive numerical simulations to explore the complex interplay between the geometrical characteristics of finned heat sinks, such as fin spacing, height, and length, and their subsequent effects on thermal and hydraulic performance. The research findings revealed that the geometrical parameters significantly impact the airflow field at the ends of the fin channels. This influence, in turn, noticeably affects the heat sink performance, especially its thermal efficacy. Rabani and Rabani [34] conducted an experimental setup to improve the thermal effectiveness of a Trombe wall. They attempted to achieve this objective by integrating rectangular fins into the design. According to their results, employing rectangular fins led to a significant enhancement (6%) in the heat transfer rate (HTR). Sathe et al. [35] conducted a study analyzing the impact of different geometric factors on the cooling effectiveness of rectangular-based finned heat sinks, applicable specifically to cooling electronic devices. Cong et al. [36] applied the principles of the constructal theory to design highly efficient rectangular fins specifically customized for electronics cooling. Moreover, Dasore et al. [37] conducted a detailed examination of internal combustion engines using numerical simulations to study how rectangular and elliptical fins affect the thermal efficiency of their air-cooled system.

Creating perforations into the fins is highly effective for optimizing various heat sinks. This technique leads to lower energy usage (pressure drop), reduced weight, and improved HTR [24]. Perforations on the surface help increase the total surface area, enhancing HTR. Additionally, strategically positioning the perforations on the fin can help reduce the resistance force and, as a result, reduce the power needed for fluid pumping. Furthermore, there is a noticeable difference in weight between fins with perforations and solid ones. In general, it can be concluded that utilizing perforated fins enables the achievement of all three desirable objectives in optimizing heat sinks.

In recent years, there has been a significant increase in the performance analysis of perforated finned heat sinks (PFHSs) through experimental and computational evaluations. In this regard, Karlapalem and Dash [38] present an optimized design for an electronics cooling type of heat sink by incorporating circular perforations to branching fins. They desired to enhance heat dissipation by fine-tuning the perforations' geometrical characteristics, such as size, spacing, and angle. The efficiency of PFHS applicable to cooling solar PV panels was analyzed by Hudişteanu et al. [39]. They simulated the influences of circle-shaped perforations on the thermal performance of PFHS. Their outcomes indicate that employing perforated fins can lead to a notable 6.49% boost in energy generation compared to the standard setup. Egab and Oudah [40] dissected the benefits of circular-shaped perforated fins for performance enhancement of Li-ion batteries. The researchers noticed that the Nusselt number of the newly designed heat sink is roughly 20% greater than that of the conventional ones. Chingulpitak et al. [41] utilized CFD simulations to find an optimized design for PFHS by varying the number and dimensions of circular perforations. According to their findings, adding 75 perforations with a 3 mm diameter could improve the HTR by 11.6%. Furthermore, they observed a significant decrease of 28% in the size of the superior PFHS.

The research indicates that both longitudinal and lateral perforations can effectively enhance the performance of heat sinks based on rectangular fins. Shaeri and Yaghoubi [42] ran CFD simulations to examine how changing the number of longitudinal channel-like perforations in a PFHS affects flow and thermal fields. Their results demonstrated that the number of perforations significantly impacts the heat dissipation and airflow resistance. Considering the turbulent airflow, Shaeri and Yaghoubi [43] accomplished additional research to simulate their earlier setup [42]. They defined a new parameter called porosity to assess how perforation volume affects the PFHS's flow and heat transfer efficiency. The researchers observed that incorporating three perforations with the highest porosity in each fin reduced weight and pressure drop and improved heat dissipation. In a separate study, Shaeri and Jen [44] utilized the highest porosity identified in Ref. [43] to examine the influence of the number of perforations on PFHS thermal and flow fields.

The capability of lateral perforations in improving the hydrothermal performance of a heat sink consisting of an array of rectangular fins was evaluated by Shahari et al. [45]. Their CFD-based analysis confirmed the significant impact of the number and porosity of lateral square-shaped openings on the performance of PFHSs. The highest level of effectiveness was observed in the PFHS with six square perforations and a porosity of 0.333. Shaeri and Bonner [46] experimentally analyze the influence of geometric characteristics of lateral perforations on thermal and flow fields of a laterally PFHS. They considered four variables associated with perforations: porosity, distance, number, and size. In order to demonstrate the superiority of PFHSs compared to solid-finned heat sinks (SFHSs), they defined a novel parameter known as mass-based thermal resistance (MBTR). They confirmed that without boosting pumping power, the MBTR of laterally PFHSs was significantly lower, ranging from 41% to 51%, compared to SFHSs. Shaeri and Bonner [47] extended their previous research on laterally PFHSs by developing analytical models based on empirical data. They consider Prandtl number, Reynolds number, fins gap size, and perforations porosity as input variables to predict the Nusselt number of PFHSs as output.

In recent years, industrial and engineering communities have experienced significant evolution under the influence of artificial intelligence (AI). There is significant potential for AI, specifically machine learning (ML), as its predominant subset in the design, control, monitoring, and optimization of heat sinks. By receiving limited information from heat sinks, ML algorithms have a remarkable ability to predict flow and thermal behavior. This feature reduces the financial costs of experiments and the computational costs of numerical simulations. Also, powerful ML-based models can act as a foundation for optimization algorithms and lead to the optimal selection of the configuration and geometrical characteristics of heat sinks. AI-based tools have the capability to aid in preventive maintenance by analyzing data from diverse sources like temperature sensors. By detecting potential issues before they escalate into critical problems, AI enhances the durability and longevity of heat sink systems.

Numerous algorithms have been developed to construct ML models, with some of the widely recognized ones being.

- Deep neural networks (DNN) [48].
- Artificial neural network (ANN) [49–53].
- Decision trees (DT) [54].
- Support vector regression (SVR) [55].
- Gradient boosting algorithm (GBA) [56].
- Gaussian process regression (GPR) [54,57,58].
- Random forest (RF) [59].
- K-nearest neighbor (K-NN) [60].
- Light gradient-boosting machine (LightGBM) [61].
- Multivariate adaptive regression splines (MARS) [62].
- Extreme gradient boosting (XG-Boost) [63].
- Adaptive neuro-fuzzy inference systems (ANFIS) [64–67].

Table 1 summarizes the most recent research focused on utilizing artificial intelligence algorithms for optimization and modeling heat sinks.

In the last two years, several AI-based analyses have been done to design, optimize, and model heat sinks. Wang et al. [68] proposed a hybrid method that combines CFD, ML, and multi-objective optimization to optimize a nanofluid mini-channel heat sink. CFD data-driven models developed using SVR, GPR, and RF methods for average temperature and pressure drop in terms of inputs (heat flow density,

Table 1
Latest research on the application of artificial intelligence algorithms for optimization and modeling of diverse heat sinks.

Authors	Year	Heat sink type	Artificial intelligence algorithms
Wang et al. [68]	2023	Mini-channel	SVR, GPR, RF, NSGA-II
Saeed et al. [69]	2023	Mini-channel	DNN, ANN, GBA, DT, RF, K-NN, GA
Tikadar et al. [70]	2022	Metal foam	ANN, SVR, XGBoost, RF, K-NN
Sikirica et al. [71]	2023	Micro-channel	ANN, GBA, RF
Shaeri et al. [72]	2022	Parallel plate	ANN and greedy search
Kim et al. [73]	2022	Micro-pin fin	LightGBM, XG-Boost, ANN
Mohammadpour et al. [74]	2022	Micro-channel	ANN, GPR, RF, K-NN
Suzuki et al. [75]	2023	Lattice-structure	RF, ANN

Reynolds number, and volume fraction). The GPR model was reported as the most suitable ML algorithm, attaining high R^2 values of 0.9985 for pressure drop and 0.9939 for average temperature prediction. The NSGA-II algorithm successfully provided optimal solutions across various operating conditions. Saeed et al. [69] employed an ML-based optimization strategy to improve the thermo-hydraulic effectiveness of a compact mini-channel heat sink. They used 3D-RANS simulations to provide CFD data as feed for their hybrid strategy. Their optimization variables were fins geometrical characteristics (height, spacing, and number) alongside Reynolds number as a fluid flow feature. Six well-known ML methods, DNN, ANN, GBA, DT, RF, and K-NN, were applied to find the best predictive models for the heat transfer coefficient and pressure drop as outputs. The superior models were coupled to GA to determine the characteristics of the optimal heat sink. The hybrid AI-based procedure demonstrated a significant performance improvement, achieving up to a 2.1 times enhancement compared to the most effective heat sink in the database. To predict metal foam heat sinks' hydraulic and thermal efficiency, Tikadar et al. [70] evaluated five ML techniques, including ANN, SVR, XGBoost, RF, and K-NN. They used a database consisting of 1000 data points generated by CFD in the modeling process. The friction factor and Nusselt number act as output variables. While Reynolds number, porosity, pore density, and heat sink geometrical parameters were considered inputs. The finding revealed that ANN, SVR, XGBoost, and RF, with mean absolute percentage error (MAPE) below 4.59%, presented precise models for predicting outputs. Nevertheless, SVR and ANN indicated predominance, particularly when tested on out-range datasets. Sikirica et al. [71] present new insights into the design of microchannel heat sinks with ribs and secondary channels. They combined CFD, ML modeling, and multi-objective optimization to minimize the thermal resistance and pumping power. They used a Latin hypercube as the design of experiments (DOE) technique for sampling. Also, ANN, GBA, and RF algorithms were applied in the optimization process. The ML-based optimization framework resulted in design points that successfully reduced the temperature by 10% compared to a traditional microchannel design while maintaining the pressure limits. Furthermore, the optimized points exhibited a remarkable reduction in pressure drop (more than 25%).

Shaeri et al. [72] aimed to optimize air-cooled parallel plate-finned heat sinks by combining ANN and greedy search algorithms. They defined their design objectives based on practical applications, which include maximizing the heat transfer coefficient ratio to pressure drop, maximizing the heat transfer coefficient within a limited flow rate, and minimizing the weight where the heat transfer coefficient is maximized within the highest permitted flow rate. They claimed that this innovative and adaptable AI-based optimization method greatly aided the practical design of parallel plate-finned heat sinks to meet various industrial requirements and accommodate diverse design specifications. Kim et al. [73] used a databank consisting of 906 data points from 15 investigations to develop valid ML models to predict the behavior of micro-pin fin heat sinks. Three ML algorithms, including LightGBM, XG-Boost, and ANN, constructed powerful relationships between thermal performance as output and geometric shape and operating conditions as inputs. The ML-based models displayed notably superior prediction accuracy, with mean absolute errors (MAEs) ranging from 7.5% to 10.9%. The results represented an around five times improvement in accuracy compared to the previous correlations. Mohammadpour et al. [74] considered a microchannel heat sink (MCHS) with double synthetic jets to determine the impacts of operational and geometrical variables on nanofluid thermal performance. In order to achieve this purpose, they combined CFD and ML algorithms (ANN, GPR, RF, and K-NN). Their inputs include jet phase actuation and insert characteristics (diameters, types, and arrangements). The findings revealed that the k-nearest neighbor model exhibited the best predictive performance compared to other evaluated ML models. An optimal combination of various input factors was suggested to minimize pressure drop and maximize heat transfer.

The previous studies [45,46] emphasized the crucial role of geometric elements of lateral perforations in the performance of finned heat sinks. These studies utilized numerical simulations to analyze the impact of perforation size and number on thermal and hydraulic performance. However, they focused on a single-objective, case-specific approach rather than a comprehensive multi-objective approach. Therefore, the absence of a comprehensive design approach for multi-objective optimization of lateral perforations in PFHSs remains a research gap. To bridge this gap, the present authors propose a novel hybrid approach that integrates computational fluid dynamics, machine learning, multi-objective optimization, and multi-criteria decision-making. This comprehensive hybrid approach aims to facilitate the optimal design of lateral perforations in finned heat sinks. The dimensions and configuration of the perforations are treated as geometric design variables, whereas the Reynolds number is considered an input variable related to the fluid flow. The design objectives are reformulated as dimensionless representations of heat transfer rate, pressure drop, and heat sink size. The redefined objectives encompass thermal performance (TP), thermo-hydraulic performance (THP), and thermo-volumetric performance (TVP). The innovative design process utilized in the present investigation has the potential to bring about a significant transformation not only in heat sink design but also in diverse engineering applications.

2. Hybrid procedure and design objectives

2.1. Proposed design strategy

The suggested hybrid strategy is composed of four distinct stages. During the initial phase, CFD is utilized to simulate the performance of the PFHSs. The objective of the first phase is to assess the influence of various design variables on the objective variables. In the second phase, the modeling process is implemented using the data acquired from the CFD simulations. For this purpose, two ML techniques, stepwise mixed selection (SMS) and GMDH-type artificial neural networks (ANN), are used. These two formula-based techniques efficiently create a relationship between the input and output variables regardless of the quality and quantity of data. In the third phase, the top-performing models obtained from the previous phase are incorporated into the MOO process using the NSGA-II algorithm. This process identifies the Pareto front, representing the optimal trade-off solutions. Finally, in the fourth phase, the desirable design for the designer is determined from the optimal points of the Pareto fronts using two well-known techniques in MCDM: TOPSIS and VIKOR. Decision-making is performed based on each objective's assigned importance coefficients (weights). Decision-making based on objective weights is one of the innovative aspects of the present study. In fact, by weighing the objectives, the designer will be able to pick the optimal design points according to the conditions and operational

requirements of the heat sink. The detailed flowchart of the described four phases of the present strategy is depicted in Fig. 1. This approach can lead to reliable results in designing laterally PFHSs, especially in applications that focus on electronics cooling systems. Detailed descriptions and outcomes of each design phase will be discussed separately in subsequent sections.

As mentioned in the introduction, the three main elements that should be considered in the design of heat sinks include HTR, pressure drop, and weight. Based on these factors, three dimensionless objectives for maximization are defined in the current research, which includes thermal performance (TP), thermo-hydraulic performance (THP), and thermo-volumetric performance (TVP). Given the criticality of heat dissipation, it is incorporated into all three objectives. In the rest of this section, these three objectives will be examined in detail.

2.2. Thermal performance (TP)

The TP measures the thermal effectiveness of PFHSs. It quantifies the extent to which HTR is enhanced by using PFHS compared to SFHS. The TP value is calculated using the following formula:

$$\mathrm{TP} = \frac{q_{pf}}{q_{sf}} \tag{1}$$

where q_{pf} and q_{sf} compute the HTR for perforated and solid fins. The equation below can be used to determine the fins' HTR:

$$q_f = \sum_i h_i \Delta A_i (T_s - T_\infty) \tag{2}$$

where T_∞ signifies the free stream temperature, and T_s symbolizes the fin's surface temperature.

2.3. Thermo-hydraulic performance (THP)

The friction drag force evaluates the hydraulic effectiveness of laterally PFHSs. The local skin friction factor is computed as follows:

$$C_f = \frac{\tau_w}{0.5\rho u_\infty^2} \tag{3}$$

The definition of wall shear stress (τ_w) is given by the following equation:

$$\tau_w = \mu \left(\frac{\partial u}{\partial n}\right)_s \tag{4}$$

Also, the average friction coefficient (AFC) is computed as follows:

$$\overline{C_f} = \frac{1}{A_T} \sum_i \left(C_f\right)_i \Delta A_i \tag{5}$$

ΔA_i denotes every solid cell interacting with the airflow, while A_T represents the total area of all solid surfaces in contact with the airflow.

A combination of hydraulic performance and thermal efficiency of PFHSs is a valuable objective in the designing process. Unifying these two critical factors in a dimensionless objective is possible as follows:

$$\mathrm{THP} = \frac{q_{pf}/q_{sf}}{\left(\overline{C_{f,pf}}/\overline{C_{f,sf}}\right)^{1/3}} \tag{6}$$

where $\overline{C_{D,sf}}$ and $\overline{C_{D,pf}}$ represent the ADC for the solid and perforated finned heat sinks, respectively.

2.4. Thermo-volumetric performance (TVP)

Similar to the THP, simultaneously considering the heat sink size and its thermal effectiveness in one factor leads to a valuable criterion. Merging these two factors into one objective is formulated as follows:

$$\mathrm{TVP} = \frac{q_{pf}/q_{sf}}{V_{pf}/V_{sf}} \tag{7}$$

where V_{sf} and V_{pf} signifies the volume of SFHS and PFHS.

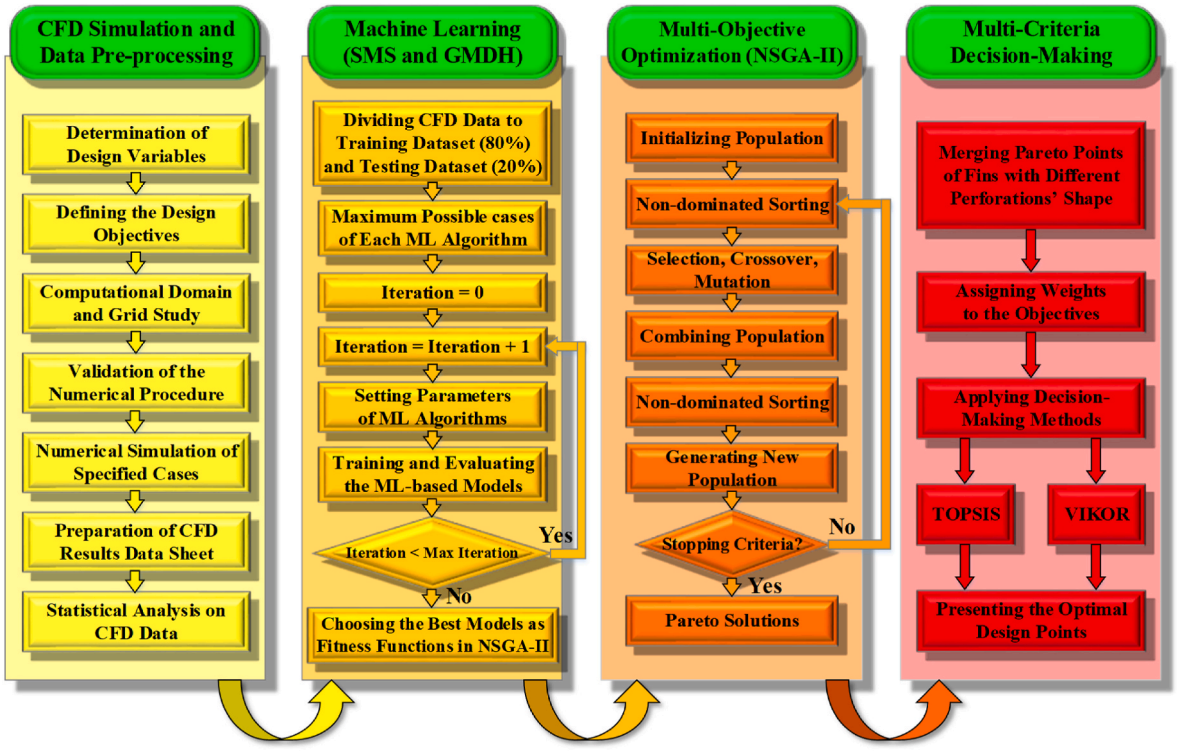

Fig. 1. General schematic of the hybrid strategy utilized in this study.

3. CFD modeling

3.1. Laterally PFHS description

The prior investigation [45] showed that the laterally PFHS with six perforations indicates a high thermal-hydraulic potential. Therefore, the present research uses a PFHS with six perforations in the shapes of squares, circles, and hexagons. The size of perforations is defined by a variable called the perforations volume ratio (φ):

$$\varphi = \frac{\text{volume occupied by the perforations}}{\text{total volume of the solid fin}} \tag{8}$$

φ is evaluated in the range of 0.25–0.5 for different perforations' shapes (PSs). Fig. 2 depicts the PFHS structure and the simulated domain alongside their dimensions. In addition, Fig. 3 (a) displays the PSs applied on the lateral surface of the fins.

3.2. Assumptions and boundary conditions (BCs)

Below is a concise overview of the assumptions.

- The airflow is steady-state, turbulent, and incompressible.
- The fin's dimensions are assumed to be L = 24 mm, H = 12 mm, and D = 4 mm.
- A uniform spacing of 10 mm (2.5D) is considered between the fins.
- The heat sink is made of aluminum.
- The airflow's properties are temperature-independent.
- The specified limits for perforations' size ($0.25 \leq \varphi \leq 0.5$) are such that it leads to maintaining the turbulent flow inside the perforations.
- The low value for the maximum temperature difference of the simulated domain (<45) leads to ignoring the radiation heat transfer [76].
- The Richardson number (Gr/Re^2) is significantly less than 0.001, which leads to the neglect of natural convection.

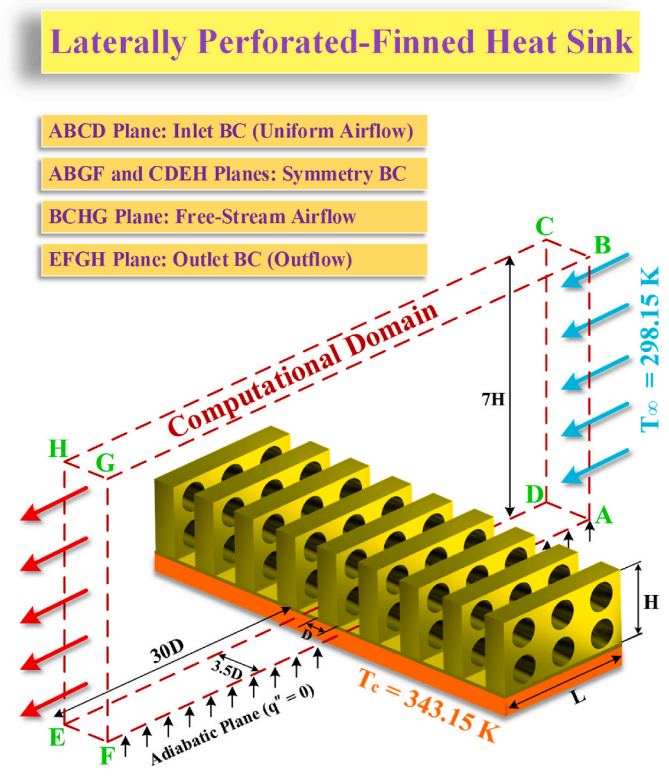

Fig. 2. The LPFHS structure and optimal simulation domain.

- Seven Reynolds numbers based on fin thickness ($Re_D = u_\infty D\nu^{-1}$) between 2000 and 5000 (interval of 500) were studied, and no instability in the flow field was observed in any of them.

Due to the symmetrical arrangement of fins and uniform airflow, the simulation focuses on a single fin [42–45,77]. In addition, previous studies [42–45,77] demonstrated that the distance between the fins and plates ABCD, EFGH, and BCHG is such that the BCs do not affect the flow and thermal fields of the fins. Based on Fig. 2, the BCs can be described as follows.

- T_∞ = 298.15 K at the free stream plane (BCHG) and the inlet BC (ABCD).
- Zero gradient (outflow) BC at outlet plane (EFGH).
- T_c = 343.15 K at the base plate of the heat sink.
- Symmetry BC on the left (CDEH) and right (ABGF) sides of the computational domain.
- The upstream and downstream plates of the fin are adiabatic ($q'' = 0$).

3.3. Governing equations and turbulent model

The governing equations of the simulated domain considering the assumptions are as follows [44,45]:

$$Continuity: \frac{\partial u_i}{\partial X_i} = 0 \tag{9}$$

$$Momentum: \frac{\partial}{\partial X_j}\left(\rho u_i u_j - \tau_{ij}\right) = -\frac{\partial P}{\partial X_i} \tag{10}$$

$$Stress: \tau_{ij} = 2\mu S_{ij} - \frac{2}{3}\mu_t \frac{\partial u_k}{\partial X_k}\delta_{ij} \tag{11}$$

$$Energy: \rho C_p \frac{\partial (u_i T)}{\partial X_i} = \frac{\partial}{\partial X_i}\left[\frac{\partial T}{\partial X_i}(\lambda + \lambda_t)\right] \tag{12}$$

$$Fourier's\ equation: \frac{\partial^2 T}{\partial X^2} = 0 \tag{13}$$

Solving the Fourier and energy equations (heat conduction and airflow convection) makes it possible to ascertain the temperature distribution on the surfaces of both the perforations and fins [45]. Additionally, expressions for S_{ij}, δ_{ij}, and μ_t are provided as follows:

$$Distortion\ rate\ tensor: S_{ij} = \frac{1}{2}\left(\frac{\partial u_i}{\partial X_j} + \frac{\partial u_j}{\partial X_i}\right) \tag{14}$$

$$Kronecker\ delta\ function: \delta_{ij} = \begin{cases} 1 & i = j \\ 0 & i \neq j \end{cases} \tag{15}$$

$$Turbulent\ viscosity: \mu_t = \frac{\rho C_\mu k^2}{\varepsilon} \tag{16}$$

Prior examinations [76,78–80] have demonstrated that the RNG k-ε turbulent model [81], an adaptation of the k-ε model, can effectively replicate important flow characteristics such as recirculation, rapid strain, streamline curvature, flow separation, and reattachment in CFD solving process.

$$Turbulent\ kinetic\ energy: \frac{\partial(\rho u_i k)}{\partial X_i} = \frac{\partial}{\partial X_i}\left(\alpha_k \mu_{eff}\frac{\partial k}{\partial X_i}\right) + \mu_t S^2 - \rho\varepsilon \tag{17}$$

$$Turbulent\ energy\ dissipation\ rate: \frac{\partial(\rho u_i \varepsilon)}{\partial X_i} = \frac{\partial}{\partial X_i}\left(\alpha_\varepsilon \mu_{eff}\frac{\partial \varepsilon}{\partial X_i}\right) + C_{1\varepsilon}\mu_t S^2 \frac{\varepsilon}{k} - C^*_{2\varepsilon}\rho\frac{\varepsilon^2}{k} \tag{18}$$

Let $C^*_{2\varepsilon}$, S, and μ_{eff} be denoted as follows:

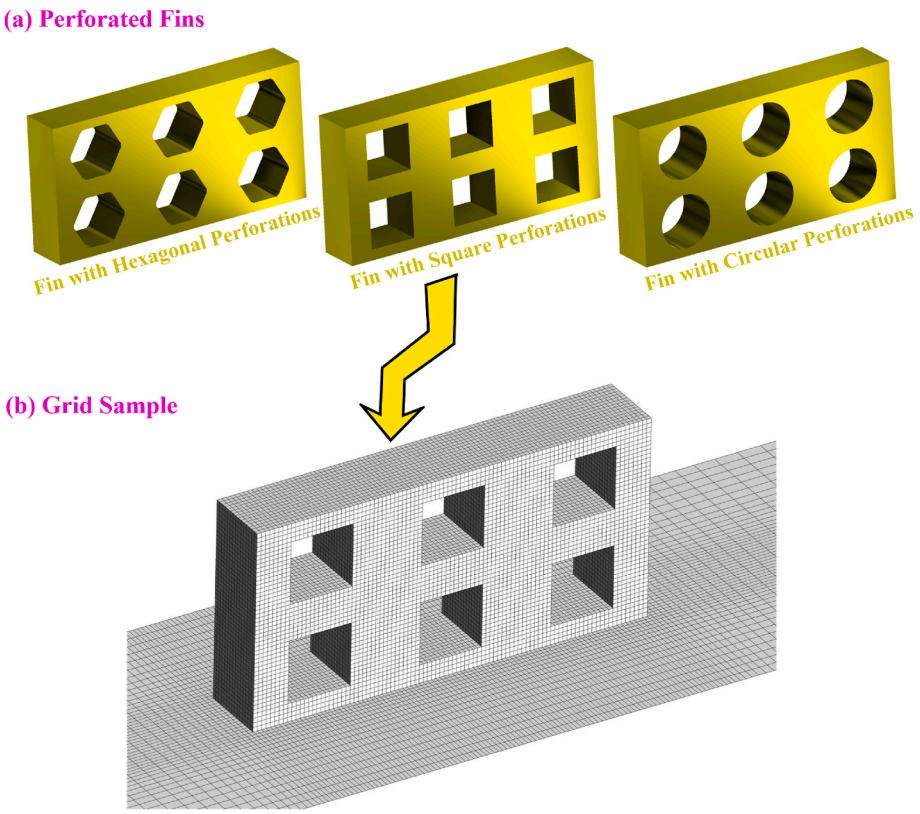

Fig. 3. (a) Various perforation types utilized in LPFHS structure and (b) sample of mesh quality for square-shaped configuration ($\varphi = 0.3$).

$$Additional\ source\ parameter: C_{2\varepsilon}^{*} = C_{2\varepsilon} + \frac{C_{\mu}\eta^{3}(1-\eta/\eta_{0})}{1+\beta\eta^{3}} \tag{19}$$

$$Mean\ rate\ of\ the\ strain\ tensor: S = \sqrt{2S_{ij}S_{ij}} \tag{20}$$

$$Effective\ viscosity: \mu_{eff} = \mu + \mu_{t} \tag{21}$$

The factor $C_{2\varepsilon}^{*}$ is responsible for differentiating between the RNG k-ε and standard k-ε models. Below are the suggested values for the constants in Eqs. (18) and (19):

$$C_{\mu} = 0.0845 \tag{22}$$

$C_{1\varepsilon} = 1.42$

$C_{2\varepsilon} = 1.68$

$\alpha_{\varepsilon} = \alpha_{k} = 1.393$

$\beta = 0.012$

$\eta_{0} = 4.38$

$\eta = Sk/\varepsilon$

3.4. Computational method

ANSYS Fluent CFD package based on the finite volume method (FVM) is employed to calculate fluid flow and thermal fields in the present computational domain. A QUICK scheme [82] is applied for discretizing governing equations, and a SIMPLE algorithm is used to calculate the pressure field, maintain mass conservation, and correlate velocity and pressure corrections. In general, the solution process can be summarized in two steps.

1. Calculate the flow field in the simulation domain by solving mass conservation, momentum conservation, k, and ε equations.
2. Resolve the thermal field in the simulation domain utilizing the information from the flow field achieved in the first step.

The energy equation reaches convergence when residual values are below 1×10^{-10}, while the criterion is set at 1×10^{-6} for other equations.

3.5. Grid analysis

In CFD simulations, reducing the cost of calculations while achieving maximum accuracy, especially in three-dimensional problems, depends on the grid study. In the present paper, five mesh grids are evaluated by various perforated fins, the results of which for a sample with square-shaped perforations are presented in Table 2.

The determination of the average Nusselt number ($\overline{Nu}$) during the grid study and validation process involves the following calculation:

$$\overline{Nu} = \frac{\overline{h}D}{\lambda} \tag{23}$$

The calculation of the average heat transfer coefficient, represented as $\overline{h}$, is performed using the following formula:

Table 2
Grid analysis for a LPFHS with square perforations ($\varphi = 0.3$ and Re = 3000).

Domain Grid size (X × Y × Z)	Perforations Grid Size (X × Y × Z)	$\overline{Nu}$	$\overline{C_f}$
146 × 70 × 36	12 × 12 × 12	15.15	0.004921
192 × 88 × 42	14 × 14 × 14	16.42	0.005631
240 × 110 × 50	16 × 16 × 16	17.37	0.006114
264 × 132 × 58	18 × 18 × 18	17.78	0.006268
300 × 148 × 64	20 × 20 × 20	17.95	0.006309

$$\overline{h} = \frac{1}{A_T}\sum_i h_i \Delta A_i \tag{24}$$

$$h = \frac{-\lambda\left(\frac{\partial T}{\partial n}\right)_S}{T_S - T_\infty} \tag{25}$$

Based on Table 2, the relative deviation of the $\overline{Nu}$ and $\overline{C_f}$ from the fourth step onwards is less than 1% and 0.7%, respectively. Hence, the 264 × 132 × 58 grid points in the X, Y, and Z directions can be considered a suitable foundation for all PFHSs. This grid structure is confirmed by implementing the grid study process on other airflow characteristics and changing the perforations' sizes and shapes. This grid for the sample with square perforations is depicted in Fig. 3 (b). In order to enhance the modeling precision of reattachment and recirculation zones, a denser grid has been implemented around the fin and perforations, as observed in the figure.

3.6. Validation

Two experimental and numerical studies are selected to check the validity of the CFD simulation implemented in the present study. For the SFHS, the experimental data of Jonsson and Moshfegh [83] were compared with the present results. Jonsson and Moshfegh tested seven types of heat sinks in the wind tunnel at 293.15 K, among which the plate-fin type heat sink had a significant similarity with the present SFHS configuration. Fig. 4 (a) illustrates the dimensions of the plate-fin type heat sink. In order to compare results, the thermal resistance is defined as follows:

$$R_{th} = \frac{1}{\overline{h} A_{hs}} \tag{26}$$

$$\overline{h} = \frac{Q}{A_{hs}(T_b - T_\infty)} \tag{27}$$

where Q represents HTR and A_{hs} symbolizes the heat transfer area. Also, Jonsson and Moshfegh defined the Reynolds number using the hydraulic diameter of the wind tunnel, which is 10 mm in height and 63 mm in width.

Fig. 4 (a) indicates that the maximum relative deviation between the experimental data and the present results is 5.4%, which reveals the high validity of the present numerical approach in predicting the flow and thermal fields for solid-type heat sinks.

Furthermore, the present SFHS and PFHSs were subjected to a validation process with the CFD work of Shaeri et al. [45]. Two parameters, namely $\overline{Nu}$ and $\overline{C_f}$, are selected to compare the results. Fig. 4 (b) presents this comparison, showing the highest relative deviation in all data points below 1%. This suggests that the present numerical procedure for analyzing laterally PFHSs is highly accurate and reliable.

4. CFD data analysis

By calculating the flow and thermal fields using CFD, the objectives of the problem (THP, TVP, and TP) can be computed in terms of design variables (PS, Re, and φ). A wide range of Reynolds numbers and the perforations volume ratio were considered to enable the exploration of the entire problem space in the modeling and optimization process.

Descriptive statistics in Table 3 characterize the datasets resulting from CFD simulations. The evaluation of skewness and kurtosis is utilized as a metric to assess the conformity of variables to a normal distribution. The level of normality exhibited by the variables is crucial as it greatly influences the complexity, time, and computational cost involved in the modeling process. Earlier studies [84–86] suggest that kurtosis in the range of −2 to 2 and skewness in the range of −1 to 1 can indicate Gaussian (normal) distribution. Considering both criteria simultaneously, TVP, φ, and Re have Gaussian distribution. Also, skewness shows a Gaussian distribution for TP and THP, while kurtosis shows a non-Gaussian distribution, meaning a slight distinction between their mean and median. In this case, these two variables have a non-normal distribution tending to normal. Fig. 5 depicts the cumulative distribution and the frequency histogram for the objectives, which can be considered a confirmation of the closeness of the objectives' distribution to the Gaussian type.

In addition, Fig. 6 shows the effects of the shape of the perforations on the performance of the heat sinks through box plots. This visual representation clearly shows insights into the relationship between the types of perforations and each objective. Fig. 6 (a) illustrates the superior effectiveness of square perforations on thermo-hydraulic performance (THP). According to the figure, the minimum THP value for PFHSs with square perforations is greater than the median value (middle line in the box) for PFHSs with other perforations. Furthermore, the median data value for heat sinks with square perforations is greater than the maximum THP value for heat sinks based on hexagonal and circular perforations. The performance of PFHSs with circular and hexagonal perforations is similar when considering the THP objective. Fig. 6 (b) reveals that the effect of the perforations' shape on TVP is not significant. Fig. 6 (c) illustrates the square perforations-based PFHSs' thermal performance (TP) better than others. According to this objective, using circular perforations can result in less thermal efficiency.

The Pearson correlation coefficient (PCC) is a criteria used to assess the degree and direction of the linear relationship between two variables. The PCC can take values between −1 and +1. A value of +1 de-

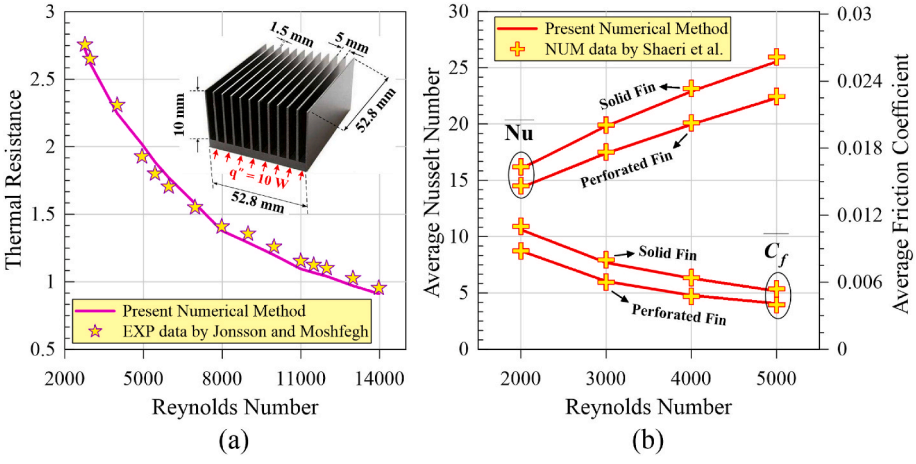

Fig. 4. Comparison of CFD results with (a) experimental data by Jonsson and Moshfegh [83], and (b) numerical data by Shaeri et al. [45].

Table 3
Descriptive statistics of objectives and design variables.

Variables		Descriptive Statistics					
		Minimum	Maximum	Mean	Std. deviation	Skewness	Kurtosis
Outputs	**THP**	1.0919	1.1878	1.1427	0.0199	0.0512	2.781
	TVP	1.3952	2.1571	1.7141	0.2259	0.2570	1.862
	TP	1.0079	1.0946	1.0538	0.0188	−0.2200	2.774
Inputs	φ	0.25	0.5	0.375	0.0857	2.95E-15	1.731
	Re	2000	5000	3500	1003.99	0	1.750
	PS	Square, Circular, Hexagonal					

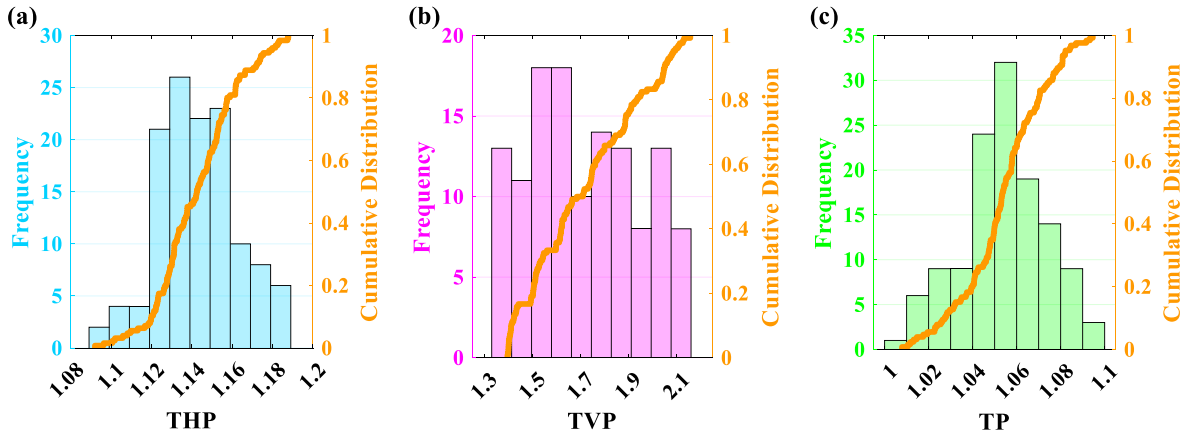

Fig. 5. The cumulative distribution and frequency histogram for (a) THP, (b) TVP, and (c) TP.

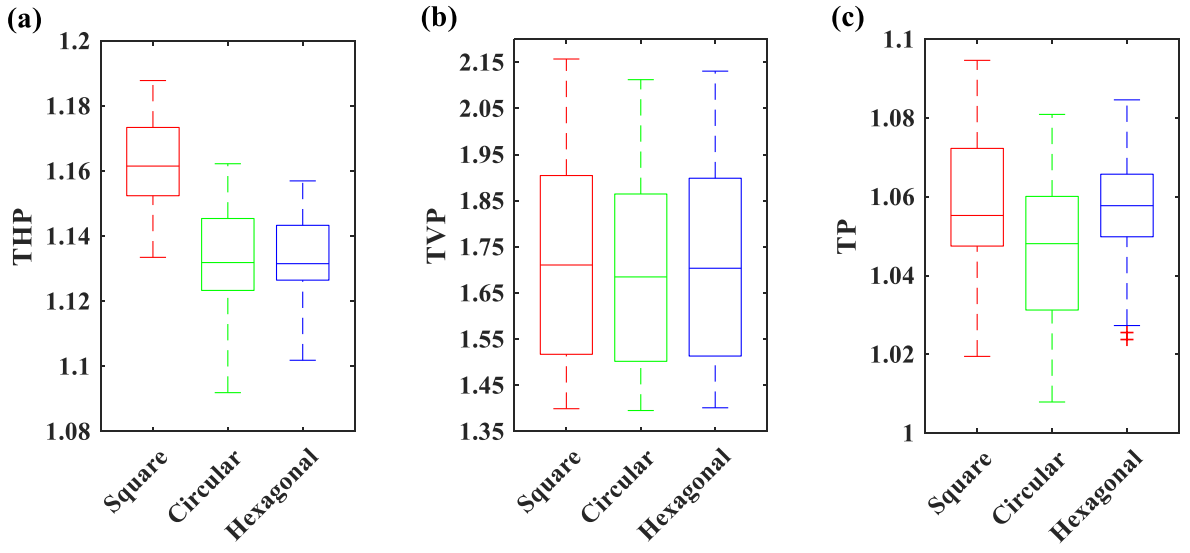

Fig. 6. Box diagrams for (a) THP, (b) TVP, and (c) TP.

notes an ideal positive linear relationship, −1 means an ideal negative linear relationship, and 0 signifies no linear relationship [87]. PCC is calculated through the following formula:

$$R_p = \frac{\sum_{i=1}^{N}(X_i - \overline{X})(Y_i - \overline{Y_i})}{\sqrt{\sum_{i=1}^{N}(X_i - \overline{X})^2 \sum_{i=1}^{N}(Y_i - \overline{Y_i})^2}} \tag{28}$$

where N, X_i, Y_i, $\overline{X}$, and $\overline{Y_i}$ represents the number of data, input variables, objectives, mean of input variables, and mean of objectives, respectively.

Fig. 7 depicts the PCC value between design variables and objectives for various perforations' shapes. According to the figure in PFHS with square perforations, the size of the perforations (φ) does not show a linear relationship with THP. For this type of perforation, THP with PCC equals −0.87, strongly depends on the Reynolds number. Significant differences are observed in the PFHSs with square and circular/hexagonal perforations. The linear dependence of THP with the φ for the PFHS with circular and hexagonal perforations equals −0.19 and −0.14, respectively. Also, the linear relationship of these perforations with the Reynolds number is less than that of square perforations, and its value is −0.82 and −0.79 for circular and hexagonal cases, respectively. On the other hand, the linear relationship between TVP and input variables is

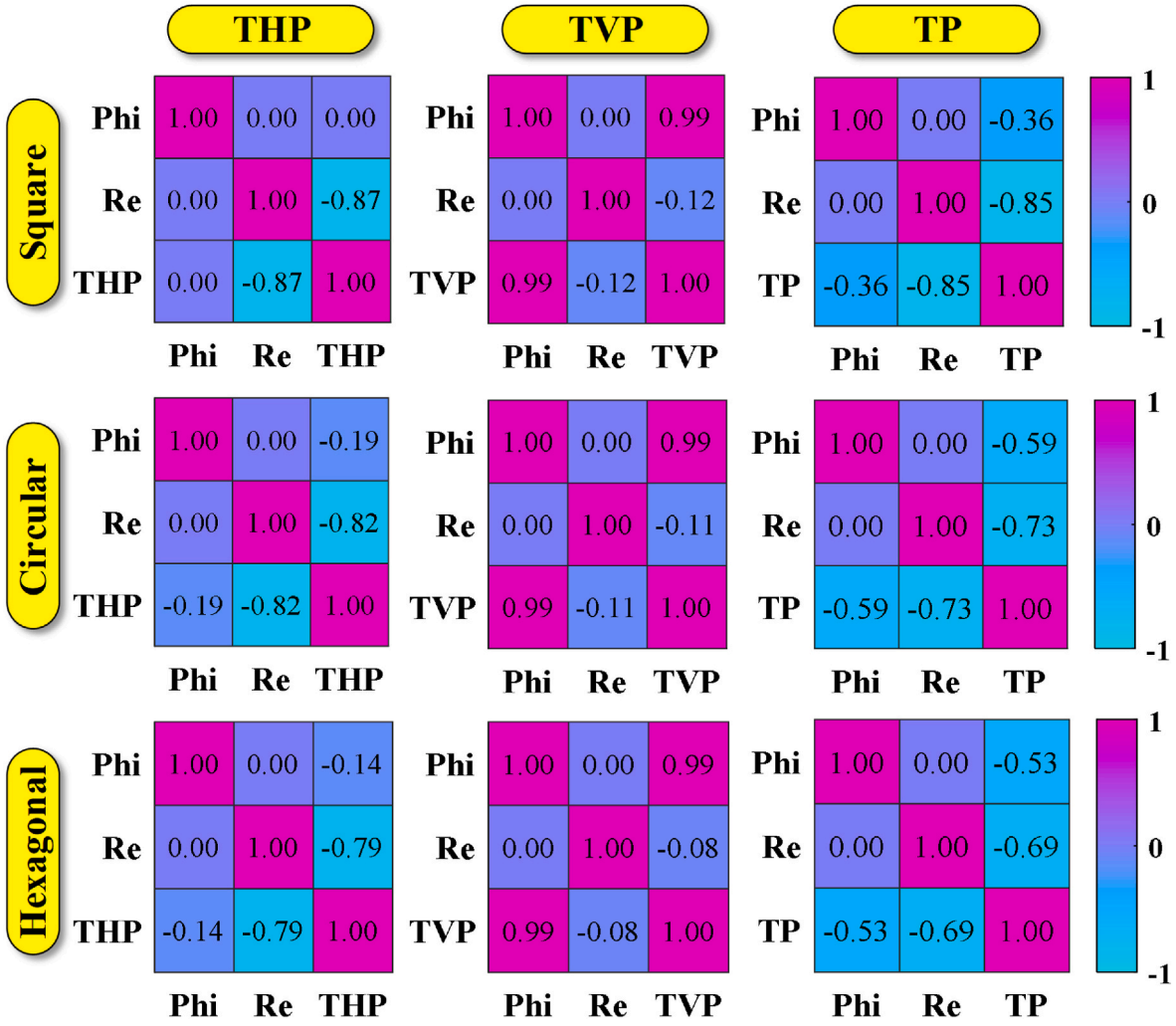

Fig. 7. Correlograms of PCC between inputs and outputs for different types of perforation.

not significantly different for the different shapes of perforations. All types of heat sinks show a linear correlation, PCC = 0.99, between TVP and φ. In contrast, the linear relationship of this objective with the Reynolds number ranges from −0.08 to −0.12. TP for different PFHSs has a relatively balanced linear relationship with φ and Re. However, its linear relationship with Reynolds number is stronger than φ. TP shows the strongest linear relationship among PFHSs with Re and φ for square-type (−0.85) and circular-type (−0.59) PFHSs, respectively. However, it is essential to note that design variables can have a non-linear correlation with objectives. Therefore, it would be imprudent to underestimate the importance of low-correlated variables.

5. Machine learning modeling

This study uses GMDH-NN and SMS techniques for ML-based modeling of objectives. GMDH-NN provides formula-based models using the advantages of neural networks, which have shown remarkable accuracy in previous research [50,88]. Despite demonstrating significant potential in this research, the SMS algorithm has received less attention. In the rest of this section, these two algorithms will be introduced, and their results will be evaluated and interpreted in modeling various objectives.

5.1. GMDH-type neural network (GMDH-NN)

The development of artificial neural networks (ANNs) can be attributed to attempts to imitate the behavior of neurons in the human brain, which led to the emergence of computational models. ANNs are affected by the quality and quantity of input data despite their high accuracy in modeling highly non-linear and complex phenomena. In order to address data-related challenges, Ivakhnenko [89] introduced the group method of data handling (GMDH) neural networks. By utilizing feed-forward neural networks, GMDH-NN not only diminishes reliance on data structure but also enhances modeling stability. A notable benefit of this ML-based technique is its ability to intelligently select effective sub-models through a self-organization process. GMDH-NN can generate formula-based models that exhibit reduced complexity while maintaining acceptable accuracy. According to the mentioned advantages, this technique has experienced significant growth in recent years [62,88,90].

In order to represent a complex phenomenon comprising M datasets, it is necessary to utilize a sophisticated function, symbolized as f, which establishes a connection between the inputs $(x_{i1}, x_{i2}, \ldots x_{in})$ and outputs y_i in the following manner:

$$y_i = f(x_{i1}, x_{i2}, \ldots x_{in}) \quad (i = 1, 2, \ldots, M) \tag{29}$$

The GMDH-NN aims to create a function, symbolized as $\widehat{f}$, that reasonably predicts the outputs. To achieve this purpose, the GMDH-NN technique seeks to minimize the difference between the real values (y_i) and the estimated values $(\widehat{y}_i)$. This can be expressed mathematically as:

$$\widehat{y}_i = \widehat{f}(x_{i1}, x_{i2}, \ldots x_{in}) \quad (i = 1, 2, \ldots, M) \tag{30}$$

$$\sum_{i=1}^{M} [\hat{y}_i - y_i]^2 \rightarrow min \tag{31}$$

Different degrees of the Kolmogorov-Gabor polynomial (Eq. (32)) [91] can be employed to designate a formula between the inputs and outputs.

$$y = \alpha_0 + \sum_{i=1}^{n} \alpha_i x_i + \sum_{i=1}^{n} \sum_{j=1}^{n} \alpha_{ij} x_i x_j + \sum_{i=1}^{n} \sum_{j=1}^{n} \sum_{k=1}^{n} \alpha_{ijk} x_i x_j x_k + \ldots \tag{32}$$

According to prior studies, it has been found that utilizing the quadratic form of Eq. (32) achieves an optimal trade-off between model accuracy and complexity [91]. The optimal form of GMDH-NN sub--models is shown in Eq. (33).

$$y = G(x_i, x_j) = a_0 + \alpha_1 x_i + \alpha_2 x_j + \alpha_3 x_i x_j + \alpha_4 x_i^2 + \alpha_5 x_j^2 \tag{33}$$

It is essential to highlight that the estimation of sub-model coefficients is accomplished using the least-squares method [92].

The GMDH technique starts modeling by constructing an input layer, where each neuron describes an input variable. These neurons serve as the initial foundation for the subsequent layers. Neurons in the intermediate layers are constructed by linking pairs of neurons from diverse layers utilizing quadratic polynomials, as defined by Eq. (33). This approach allows for extracting complex relationships and interactions between variables. A single neuron aggregates the information from the preceding layers to generate the final output in the output layer. The self-organizing procedure within GMDH concerns assessing the performance of various neurons in the intermediate layers. Neurons that contribute positively to enhancing the efficiency and accuracy of the output model are retained, while those that do not meet the desired criteria are discarded. This selective retention ensures that only the most informative and relevant neurons are incorporated into the final model.

5.2. Stepwise mixed selection (SMS)

Stepwise selection is a regression technique based on selecting input variables or terms composed of the inputs that form a robust predictive model in a self-organizing process. Influential variables, terms, or sub-models that aid in enhancing the accuracy of the model are retained within the model, while those that are not highly effective based on statistical criteria are eliminated from the model. This process leads to maintaining valuable sub-models and ignoring less essential terms, which results in reducing the model's complexity, improving its interpretability, and making it applicable in real-world applications. This approach can be particularly helpful when handling extensive data and numerous variables.

Stepwise regression has three approaches: stepwise forward selection (SFS), stepwise backward selection (SBS), and stepwise mixed selection (SMS). In the SFS approach, the model starts without any predictors, and sub-models are added to the model based on the specified accuracy threshold. This process continues until no other sub-model satisfies the target threshold. On the other hand, in the SBS approach, the modeling process starts by considering potential sub-models. It continues by eliminating the less important ones until the defined threshold does not lead to the elimination of another sub-model. The SMS approach combines forward and backward selections, which is inherently more complex. However, higher accuracy is one of its notable features. The modeling process in this study utilizes the SMS approach.

In the present study, an improved version of the SMS approach is developed, which is able to lead to accurate models in four steps as follows.

1. Production of various sub-models using the following relationships that provide significant diversity by combining input variables to increase accuracy in modeling.

$$y = \sum_{i=1}^{n} \beta_i g(x_i) \tag{34}$$

$$y = \sum_{i=1}^{n} \sum_{j=1}^{n} \beta_{ij} g(x_i) \bullet g(x_j) \tag{35}$$

$$y = \sum_{i=1}^{n} \sum_{j=1}^{n} \beta_{ij} g(x_i) / g(x_j) \tag{36}$$

The function g applies a diverse set of operators on variables. In fact, the improved form of the variables joins the modeling process, which can record a better correlation with the outputs. These operators include square root, cube root, exponential, trigonometric, sigmoid, and so on.

2. The least squares technique calculates the coefficients of the sub-models in the training process.
3. The root mean square error (RMSE) validation measure compares sub-models' accuracy throughout the validation procedure.
4. The final model is created by mixing the most effective sub-models while ensuring the complexity remains within the specified limits.

Due to the imposition of multiple sub-models and numerous operator functions, the SMS approach often incurs significant computational costs and tends to generate intricate models. To address this issue, it is necessary to limit the complexity of the model by restricting the number of permissible sub-models. Nevertheless, it is evident that reducing complexity results in a decrease in accuracy. Therefore, balancing accuracy and complexity can be a serious challenge. Implementing a series of trial-and-error analyses for this objective can be very effective.

5.3. Models development and assessment criteria

Fig. 1 depicts the procedure of selecting optimal models for both modeling techniques. The whole search strategy (WSS) is employed to optimize hyper-parameters and make structural adjustments for ML techniques. Implementing WSS on the SMS approach leads to selecting the optimal operators for each input variable, finding the optimal sub-models based on the combination of variables, and determining the optimal number of additive sub-models. In addition, a trial and error analysis was implemented to find a reasonable complexity that leads to appropriate precision. This analysis indicated that a maximum of nine sub-models can achieve high accuracy. In fact, this limitation leads to the development of uncomplicated yet powerful models that can give high credibility to the optimization results.

On the other hand, the GMDH-NN output models' precision is strongly affected by the number of layers and neurons in each layer. GMDH-NN produces extremely complex models if these two parameters are not bound. To ensure a fair comparison between the two ML techniques, they must have a similar level of complexity. Through trial and error analysis, it was determined that setting the number of layers to 2 and the number of neurons in each layer to 1 can achieve an equivalent level of complexity to the SMS method. In addition to making the two methods comparable, these limitations lead to significant simplicity in the models that can be implemented in real-world applications.

The CFD datasets in the modeling process are divided into two parts, which include 80% for training the models and the remaining 20% for evaluating the models and ranking them in the WSS process. For the fair implementation of the training and testing process, fixed train and test datasets are used for both algorithms. Also, a subset of the training data set is used for validation in the modeling process, whose task is to prevent overtraining and evaluate the generalization ability of the models. The validation process employs a leave-one-out cross-validation approach.

In order to evaluate and compare developed models, several statistical criteria are used. These criteria use the number of data points (n),

CFD values ($Y_{i,CFD}$), and predicted values ($Y_{i,Pred}$) and are defined as follows [25,93,94]:

$$\text{Root mean squared error}: RMSE = \sqrt{\frac{1}{n}\sum_{i=1}^{n}\left(Y_{i,CFD} - Y_{i,Pred}\right)^2} \tag{37}$$

$$\text{Mean absolute percentage error}: MAPE(\%) = \frac{1}{n}\sum_{i=1}^{n}\left|\frac{Y_{i,Pred} - Y_{i,CFD}}{Y_{i,CFD}}\right| \times 100 \tag{38}$$

$$\text{Correlation coefficient}: R = \frac{\sum_{i=1}^{n}\left(Y_{i,CFD} - \overline{Y_{i,CFD}}\right)\left(Y_{i,Pred} - \overline{Y_{i,Pred}}\right)}{\sqrt{\sum_{i=1}^{n}\left(Y_{i,CFD} - \overline{Y_{i,CFD}}\right)^2 \sum_{i=1}^{n}\left(Y_{i,Pred} - \overline{Y_{i,Pred}}\right)^2}} \tag{39}$$

$$\text{Coefficient of determination}: R^2 = 1 - \sum_{i=1}^{n}\frac{\left(Y_{i,Pred} - Y_{i,CFD}\right)^2}{Y_{i,CFD}^2} \tag{40}$$

The agreement degree between predicted and CFD data can be evaluated by utilizing the correlation coefficient (R) and coefficient of determination (R^2), which have values ranging from 0 to 1. Higher values of R and R^2 indicate more accurate models, while values closer to zero suggest an unreliable model. Furthermore, MAPE and RMSE offer valuable information about the errors in the models, and when these values approach zero, it indicates a high level of precision.

5.4. Modeling results

This sub-section presents the best output models from WSS applied to ML techniques for various objectives. The performance of both ML techniques for different perforations is evaluated using statistical criteria and regression graphs. Finally, the models that have the best accuracy are selected to participate in the optimization process.

5.4.1. Thermo-hydraulic performance (THP)

Table 4 presents different criteria for the best WSS-based ML models in predicting THP. According to the table, both models provide reliable results. However, the accuracy of the SMS approach in predicting THP is much better than GMDH-NN, especially in the case of PFHS with square perforations. In the testing phase, the SMS-based models show high correlation coefficient (R) values of 0.999743, 0.997620, and 0.996580 for square, circular, and hexagonal perforations. GMDH-NN models achieve 0.995584, 0.994248, and 0.995475 R-values for square-, circular-, and hexagonal-based PFHS, respectively.

The principal benchmark for comparing data-driven models is based on the results of the testing phase. Nevertheless, comparing the training phase results is not futile and can provide insights into the performance of the models during the training process. By comparing the outcomes of the training phase, it is clear that the SMS method, like the testing phase, is significantly superior to the GMDH-NN method. During the training phase, the SMS-based models show R-values of 0.999545, 0.998706, and 0.998376 for PFHS with square, circular, and hexagonal perforations. In contrast, the GMDH-NN models demonstrate R-values of 0.989156, 0.990946, and 0.985251 for square-, circular-, and hexagonal-based PFHS, respectively.

Fig. 8 illustrates the values of the CFD data points compared to their predicted values by SMS and GMDH-NN techniques for the training and testing stages. A quick examination of Fig. 8 reveals that the SMS-based models' results in all the perforations' shapes deviate slightly from the Y = X line. This observation validates the strong correspondence between the actual and predicted values, indicating the high accuracy of these models. Table 5 presents the best models' formula in predicting THP for various PSs.

5.4.2. Thermo-volumetric performance (TVP)

Table 6 presents the statistical criteria of the best SMS and GMDH-NN models for TVP prediction. The table's findings indicate the SMS approach's higher accuracy in predicting TVP for PFHSs with square (R = 0.999996) and circular (R = 0.999934) perforations. Meanwhile, the GMDH-NN method with an R-value of 0.999966 slightly better predicts PFHSs with hexagonal perforations than the SMS approach (R = 0.999939). The visible trend is different in the training phase, where the SMS method performs much better than the GMDH-NN method in predicting the THP of perforated finned heat sinks with square (R = 0.999991), circular (R = 0.999944) and hexagonal (R = 0.999990) perforations.

Fig. 9 depicts the regression plots of the best SMS and GMDH-NN models in TVP prediction. As can be seen, the testing and training data points in both approaches have high compliance with the Y = X line, indicating the high reliability of both models. However, focusing on the figure's details indicates the deviation of several data points of GMDH-NN from the Y = X line, especially in cases with square and circular perforations. Table 7 shows the developed relationships between TVP and inputs for the top models predicting TVP.

5.4.3. Thermal performance (TP)

Table 8 presents the value of statistical criteria in the testing and training stages for evaluating TP predictive models for the SMS and GMDH-NN methods. Both approaches demonstrate satisfactory accuracy; however, as seen in the previous objective, the SMS method outperforms in predicting the TP of heat sinks with square and circular perforations. While for heat sinks with hexagonal perforations, the GMDH-NN has a higher ability. The SMS-based model for cases with square, circular, and hexagonal perforations provides the R-value of 0.999592, 0.992566, and 0.995796, respectively. In contrast, the GMDH-NN model reports values of 0.998366, 0.990823, and 0.998058, respectively. During the training phase, the SMS method displays lower error rates in TP-values prediction. The R-values of 0.999673, 0.995510, and 0.999290 in the training stage are reported for heat sinks based on square, circular, and hexagonal perforations, respectively. Nevertheless,

Table 4
Statistical criteria of the best SMS and GMDH-NN models for THP prediction.

Data	PS	ML method	RMSE	MAPE (%)	R	R^2
Testing Dataset	Square	**SMS**	**0.000331**	**0.02458**	**0.999743**	**0.999387**
		GMDH	0.001634	0.09553	0.995584	0.985040
	Circular	**SMS**	**0.001449**	**0.08925**	**0.997620**	**0.992566**
		GMDH	0.002810	0.15055	0.994248	0.972034
	Hexagonal	**SMS**	**0.001228**	**0.08350**	**0.996580**	**0.991245**
		GMDH	0.001336	0.09339	0.995475	0.989641
Training Dataset	Square	SMS	0.000405	0.02880	0.999545	0.999090
		GMDH	0.001973	0.13711	0.989156	0.978430
	Circular	SMS	0.000832	0.05665	0.998706	0.997413
		GMDH	0.002195	0.15883	0.990946	0.981975
	Hexagonal	SMS	0.000717	0.05529	0.998376	0.996754
		GMDH	0.002153	0.16013	0.985251	0.970719

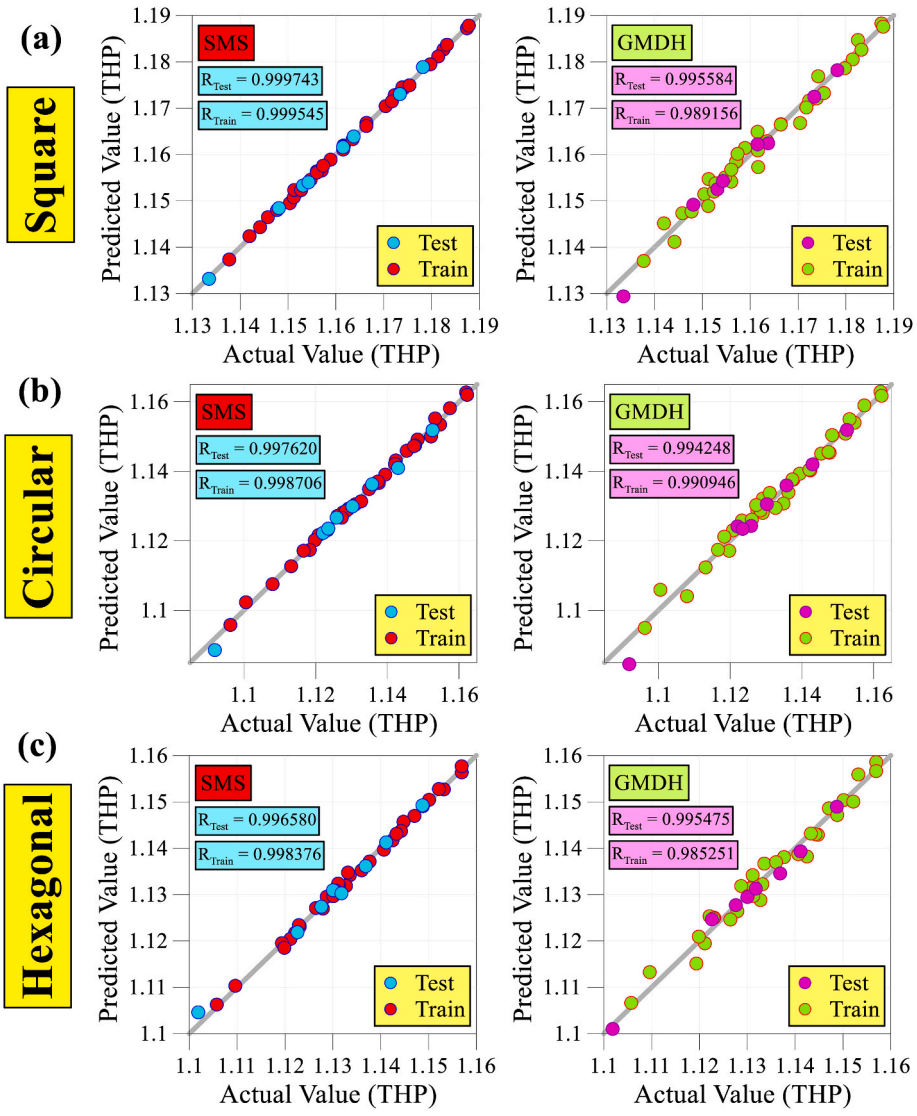

Fig. 8. The regression plots of the best SMS and GMDH-NN models for THP prediction.

Table 5
The formula of the optimal ML models for THP prediction.

PS	Best ML method	Formula
Square	SMS	$THP_{\text{Square}} = 1.42404 + Re^{1/3} * \ln Re * 0.00924377 + \varphi * \ln \varphi * (-1.07833) + \sin(Re) * \cos(Re) * (-0.0060223) + \varphi * Re^2 * 1.59589e-08 + \ln Re * \cos(\varphi) * (-0.18117) + Re * e^{\varphi} * (-0.00011019) + Re^{1/3} * \ln \varphi * (-0.00440047) + \sin(Re) * \cos(\varphi) * 0.00092409$
Circular	SMS	$THP_{\text{Circular}} = 1.03358 + Re * e^{\varphi} * 3.42215e-05 + Re * \varphi^{1/3} * 2.14718e-06 + \varphi^2 * 0.417151 + Re * Re^{1/3} * (-1.58281e-06) + Re^{1/3} * \sin(\varphi) * 0.660363 + \varphi * Re^{1/3} * (-0.556406) + \sin(Re) * \cos(Re) * (-0.0079316) + Re^{1/2} * \sin(\varphi) * (-0.0254571)$
Hexagonal	SMS	$THP_{\text{Hexagonal}} = -12.6156 + Re * \varphi^{1/3} * 0.000179339 + \varphi^2 * 71.5597 + Re * Re^{1/2} * (-8.556e-07) + \sin(Re) * \cos(Re) * (-0.00834486) + \varphi * \cos(\varphi) * 41.9974 + \varphi * Re^{1/3} * (-0.110057) + \varphi * \varphi^{1/3} * (-99.4513) + e^{\varphi} * \cos(\varphi) * 12.0258$

R-values for GMDH-NN models are equal to 0.997602, 0.993577, and 0.997399, respectively.

Fig. 10 compares the compliance level of predicted values for TP with actual values for all data points using the two ML methods. According to Fig. 10 (a), it is clear that for the heat sinks with square perforations, the data points in the SMS approach have less deviation from the Y = X line, which shows its higher precision compared to GMDH-NN. Fig. 10 (b) depicts a significant similarity between the distributions of data points of both methods for PFHSs with circular perforations. However, the data points of the SMS approach yield less error. Fig. 10 (c) displays the performance of two ML methods for heat sinks based on hexagonal perforations. According to the figure, the SMS method develops a low error model in the training phase. However, it does not perform well in the evaluation stage, and the predictive model obtained from the GMDH-NN indicates a better performance. Table 9 presents the best TP predictive models for different PSs.

6. Multi-objective optimization

The optimization of the perforated finned heat sink defined in the present research relies on the maximization of three redefined dimensionless objectives. In fact, maximizing the three objectives leads to maximizing the HTR, minimizing the volume (weight) of the heat sink,

Table 6
Statistical criteria of the best SMS and GMDH-NN models for TVP prediction.

Data	PS	ML method	RMSE	MAPE (%)	R	R^2
Testing Dataset	Square	**SMS**	**0.000798**	**0.03960**	**0.999996**	**0.999989**
		GMDH	0.004892	0.21798	0.999854	0.999576
	Circular	**SMS**	**0.002675**	**0.13673**	**0.999934**	**0.999861**
		GMDH	0.008814	0.36167	0.999382	0.998493
	Hexagonal	SMS	0.002667	0.08578	0.999939	0.999869
		GMDH	**0.002138**	**0.10960**	**0.999966**	**0.999916**
Training Dataset	Square	SMS	0.000955	0.04413	0.999991	0.999982
		GMDH	0.003176	0.15024	0.999902	0.999804
	Circular	SMS	0.002286	0.10667	0.999944	0.999888
		GMDH	0.004977	0.21868	0.999735	0.999470
	Hexagonal	SMS	0.001025	0.05040	0.999990	0.999979
		GMDH	0.002621	0.12632	0.999931	0.999863

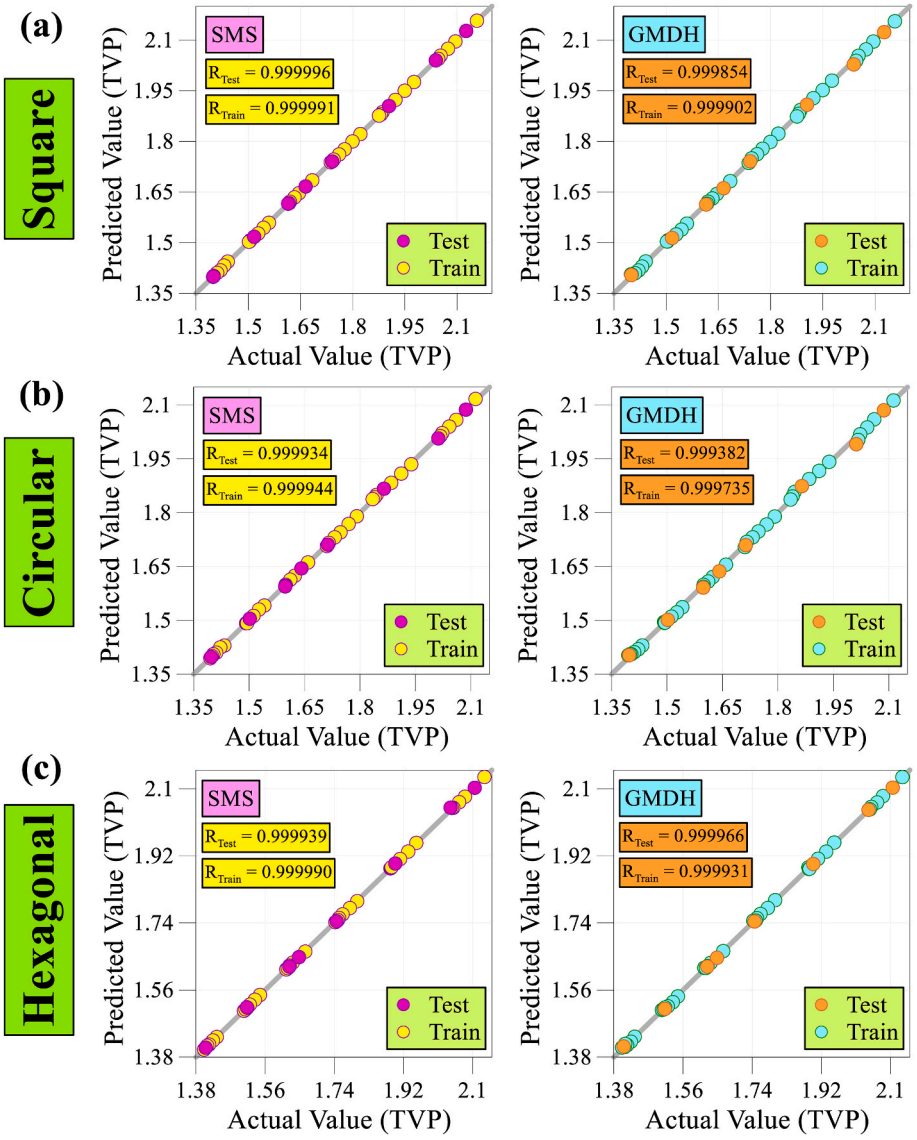

Fig. 9. The regression plots of the best SMS and GMDH-NN models for TVP prediction.

and minimizing the pressure drop (friction coefficient). Hence, it is advisable to search for circumstances where the design variables align in a way that optimizes all three objectives simultaneously. For this purpose, multi-objective optimization based on the Pareto front is a reliable solution. In contrast to traditional methods that identify a single optimal value, the Pareto approach suggests a set of optimal points, offering a range of possible solutions. These points do not have a superiority over each other, and their distinction lies in the relative significance of the objectives. The designer is responsible for selecting the optimal point to incorporate into the design based on the relative importance of the objectives. In the rest of this section, the well-known and widely used NSGA-II algorithm presented by Deb et al. [95] is introduced and used to

Table 7
The formula of the optimal ML models for TVP prediction.

PS	Best ML method	Formula
Square	SMS	$TVP_{Square} = 5.73484 + \varphi * \sin(\varphi) * (-34.8264) + \varphi * Re^{1/2} * (-0.684225) + \sin(\varphi) * Re^{1/2} * 0.0685165 + \varphi * Re * 0.00149137 + \varphi * e^{\varphi} * 14.6994 + \varphi^{1/3} * (-13.7521) + Phi * Re^{1/3} * 2.5252 + Re * \cos(Re) * 3.97945e-07$
Circular	SMS	$TVP_{Circular} = -7934.97 + \varphi^2 * 3371.32 + \varphi * Re^{1/2} * 0.0877912 + Re^{1/2} * \sin(\varphi) * (-0.107858) + (\cos(Re))^2 * 0.00271193 + Re * \cos(Re) * 6.28213e-07 + \cos(\varphi) * 9145.66 + (\cos(\varphi))^2 * (-1209.49) + Re^2 * 4.3975e-09$
Hexagonal	GMDH-NN	$TVP_{Hexagonal} = 0.558082 + \varphi * 1.71864 - \varphi * f * 0.932039 + f^2 * 0.377632$ $f(\boldsymbol{\varphi}, \boldsymbol{Re}) = 1.21893 + \varphi * 0.538422 - \varphi * Re * 7.55698e-05 + \varphi^2 * 3.1362 - Re * 5.52982e-05 + Re^2 * 9.51404e-09$

Table 8
Statistical criteria of the best SMS and GMDH-NN models for TP prediction.

Data	PS	ML method	RMSE	MAPE (%)	R	R^2
Testing Dataset	Square	**SMS**	**0.000502**	**0.03749**	**0.999592**	**0.999114**
		GMDH	0.001385	0.11580	0.998362	0.993245
	Circular	**SMS**	**0.002218**	**0.18928**	**0.992566**	**0.983757**
		GMDH	0.002892	0.21669	0.990823	0.972385
	Hexagonal	SMS	0.001587	0.08626	0.995796	0.986031
		GMDH	**0.001318**	**0.10406**	**0.998058**	**0.990358**
Training Dataset	Square	SMS	0.000488	0.03617	0.999673	0.999345
		GMDH	0.001318	0.09208	0.997602	0.995223
	Circular	SMS	0.001905	0.13912	0.995510	0.991039
		GMDH	0.002277	0.16714	0.993577	0.987195
	Hexagonal	SMS	0.000562	0.04616	0.999290	0.998580
		GMDH	0.001075	0.08534	0.997399	0.994804

determine Pareto optimal points.

6.1. Non-dominated sorting genetic algorithm II (NSGA-II)

NSGA-II is an evolutionary algorithm that effectively overcomes the limitations of prior algorithms by integrating various crucial features, including.

1. Non-Dominated Sorting: NSGA-II employs a non-dominated sorting approach to classify individuals into distinct fronts, considering their dominance relationships. This approach ensures the preservation of a diverse range of solutions.
2. Crowding Distance: NSGA-II incorporates the concept of crowding distance as a metric to maintain the diversity of solutions within each front. This technique guarantees that solutions are evenly spread across the Pareto front, promoting a balanced representation.
3. Elitism: NSGA-II integrates elitism by transferring the top-performing individuals from generation to generation. This mechanism ensures the preservation of the best solutions and prevents premature algorithm convergence.
4. Tournament Selection: In NSGA-II, tournament selection compares a random subset of individuals based on their fitness values. This approach guarantees a fair selection procedure and promotes the exploration of the search space by considering a diverse range of individuals.
5. Genetic Operators: NSGA-II utilizes typical genetic operators, such as mutation and crossover, to generate new offspring solutions. These operators play a crucial role in effectively exploiting and exploring the search space, allowing for the discovery of potentially optimal solutions.
6. Pareto Dominance: NSGA-II employs Pareto dominance to compare potential optimal points. This technique guarantees that the obtained solutions considering all objectives do not dominate each other, which results in a set of non-dominated solutions.

For more detailed information, readers can refer to the work of Deb et al. [95]. Fig. 11 provides a visual representation of the step-by-step optimization process employed by the NSGA-II algorithm. The mathematical formulation of the current multi-objective optimization problem is as follows:

$$\begin{cases} Maximize\ THP = f_1(Re, \varphi) \\ Maximize\ TVP = f_2(Re, \varphi) \\ Maximize\ TP = f_3(Re, \varphi) \\ Subject\ to \begin{cases} 0.25 \le \varphi \le 0.5\ (Real) \\ 2000 \le Re \le 5000\ (Real) \end{cases} for\ various\ PFs \end{cases} \quad (41)$$

6.2. MOO results

Fig. 12 depicts the Pareto fronts for PFHSs based on different perforations' shapes regarding various objectives. As it is known, the different shapes of the perforations provide a wide range of optimal points, each of which achieves optimization conditions according to the relative importance of the objectives. Since the optimal design means maximizing all three objectives, with a quick look at Fig. 12, it can be seen that heat sinks based on square perforations provide more significant performance than other PFHSs. This is because the square-based PFHSs demonstrate a tendency for their Pareto points to approach the upper right region, which represents the region of ideal solutions. According to this preliminary analysis, PFHSs with circular and hexagonal perforations reveal similar performance due to the entanglement of their Pareto points. By analyzing the optimal points' distribution with respect to the input variables, as depicted in Fig. 13, one can gain a holistic comprehension of the variations in the optimal values of the design variables.

Fig. 13 shows the optimal range for design variables (Re and φ) for different types of PFHSs. As can be seen, the optimal points of PFHS with square perforations indicate the value of φ in the range of 0.36–0.5. While φ-value in the optimal points of heat sinks based on circular and hexagonal perforations are distributed in the range of 0.25–0.5 and 0.33 to 0.5, respectively. These values indicate that heat sinks featuring square perforations exhibit optimal points concentrated within a narrower φ range. In contrast, heat sinks based on circular perforations provide optimal points in all possible spaces for φ. On the other hand, the Reynolds number experiences a minimal range of optimal values for

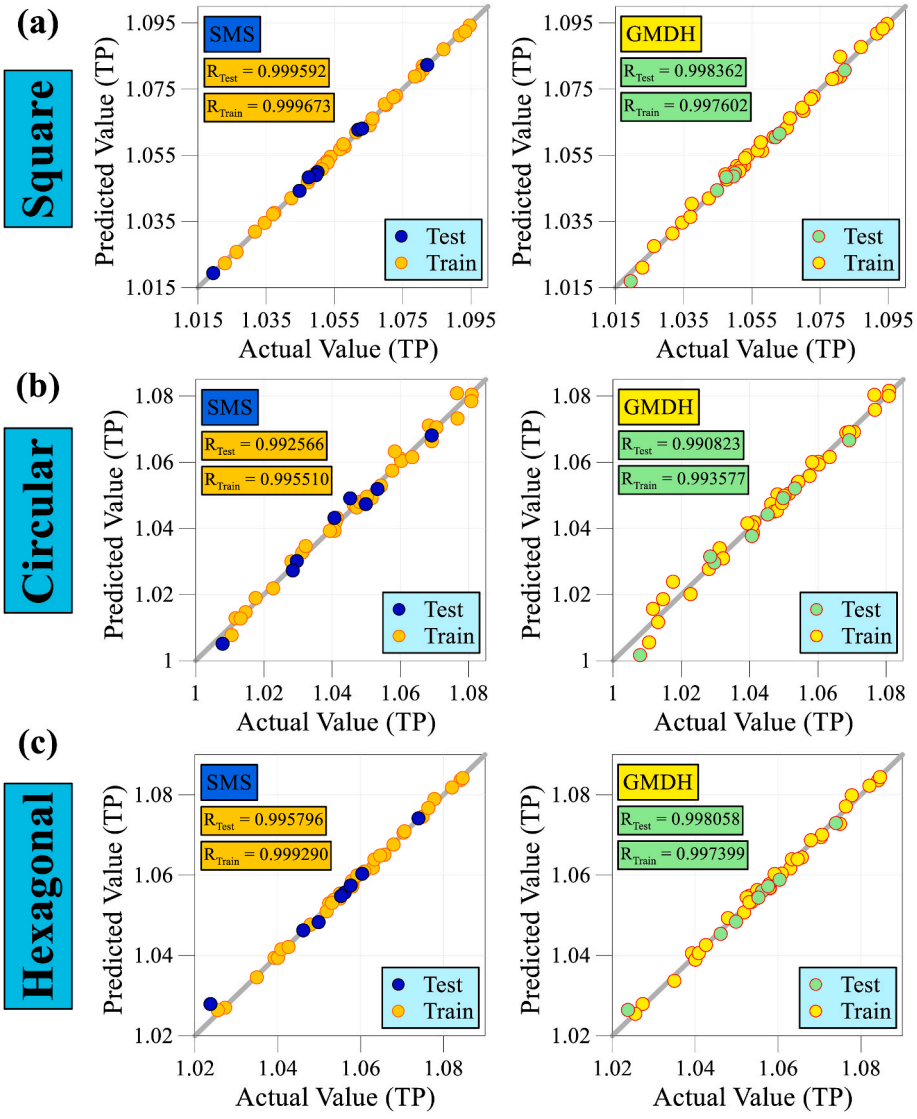

Fig. 10. The regression plots of the best SMS and GMDH-NN models for TP prediction.

Table 9
The formula of the optimal ML models for TP prediction.

PS	Best ML method	Formula
Square	SMS	$TP_{Square} = 0.626898 + e^{\varphi} * Re^{1/2} * 0.00529239 + \sin(Re) * \cos(Re) * (-0.00486598) + \cos(\varphi) * \varphi^{1/3} * 1.1262 + \sin(\varphi) * Re^{1/3} * (-0.0966089) + Re * \cos(Re) * 2.55341e-07 + \cos(\varphi) * Re^{1/3} * (-0.0261962) + \sin(\varphi) * \cos(\varphi) * 0.308208 + \varphi * Re * 1.84236e-05$
Circular	SMS	$TP_{Circular} = 1.13382 + \varphi * Re * (-0.280548) + (\sin(\varphi))^2 * 0.00205578 + \sin(Re) * \cos(Re) * (-0.00504611) + Re * \sin(\varphi) * 0.180209 + Re * e^{\varphi} * 0.098701 + Re * \cos(\varphi) * 0.0840893 + Re * (-0.182692) + Re^2 * 3.57856e-09$
Hexagonal	GMDH-NN	$TP_{Hexagonal} = -2.05461 - Re * 3.37295e-06 + Re^2 * 4.16084e-10 + f * 4.934 - f^2 * 1.87686\, f(\varphi, Re) = 1.06647 + \varphi * 0.514015 - \varphi * Re * 2.78355e-05 - \varphi^2 * 0.677185 - Re * 4.12215e-05 + Re^2 * 5.93531e-09$

different types of PFHS. Reynolds optimum points for square-based PFHS are in the range of 2000<Re<2004. For circular-based PFHSs, the value of Reynolds number of optimal points changes in an extremely limited range, between two values of 2000 and 2001. In addition, Reynolds' optimum points for heat sinks with hexagonal perforations are reported to be similar to the square-based case.

Focusing on the details of the Pareto front indicates the presence of 54% of Pareto points in φ-values greater than 0.45 for PFHSs with square perforations. Meanwhile, for circular and hexagonal perforations, 26% and 33% of Pareto points are present in the mentioned range, respectively. This finding proves the possibility of recognizing the heat sink as the optimal case by increasing the size of the square perforations. The reverse of this trend is evident for circular perforations, where more than 50% of the optimal points have φ less than 0.4. This report highlights the dependence of the perforations' size on their shape in optimal conditions.

According to Fig. 13, the optimal Reynolds number experiences an almost constant value around the minimum possible value (2000). Meanwhile, the optimal points accept a wide range of φ. By increasing the size of the perforations at the optimal points, the THP first increases and then decreases. The highest yield for THP is obtained at the value of 1.1875, whose φ equals 0.43. Meanwhile, the maximum efficiency of

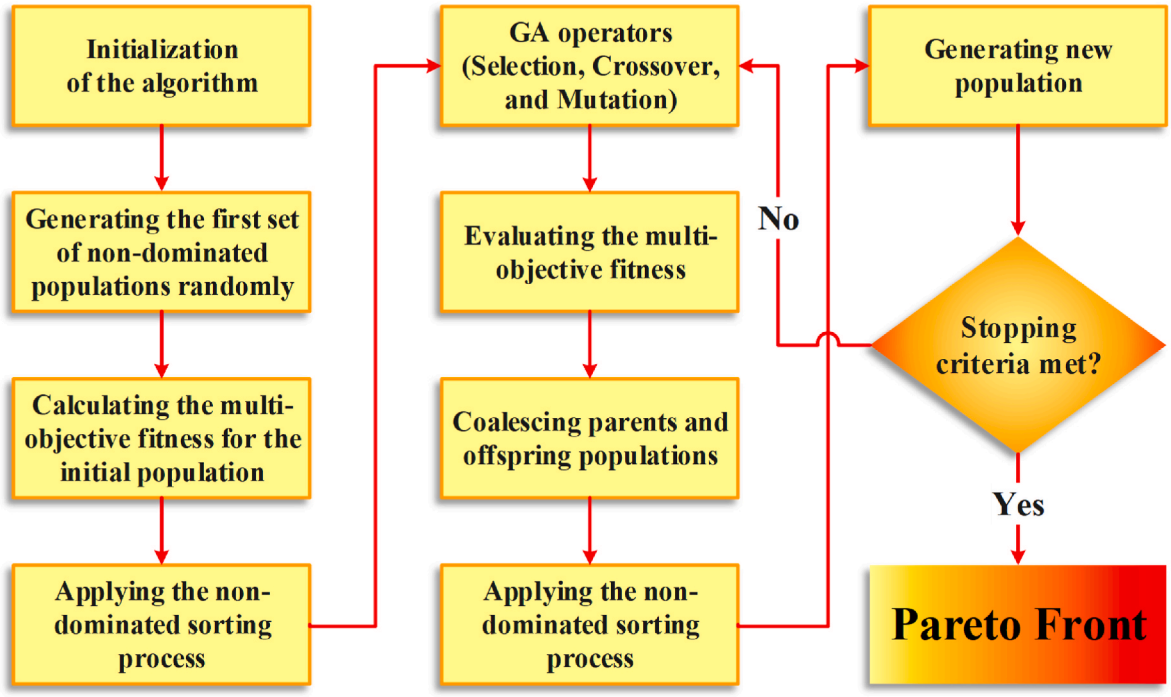

Fig. 11. Flowchart of NSGA-II algorithm.

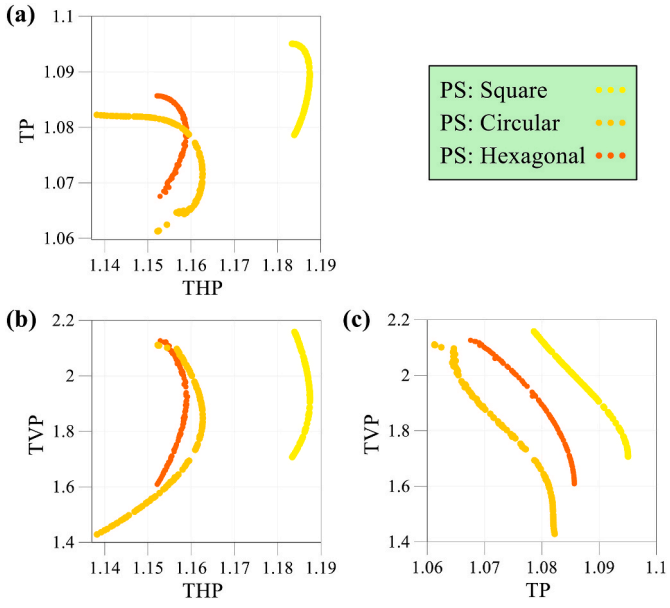

Fig. 12. Pareto optimal points for LPFHSs with various perforation types.

THP for circular- and hexagonal-based PFHSs is 1.163 and 1.159, respectively, which occurs at φ equal to 0.42 and 0.44. Moreover, based on the results presented in Fig. 13, regardless of the shape of the perforations, TVP and TP reach their maximum efficiency at the highest and lowest possible optimal φ-value, respectively.

7. Multi-Criteria Decision-Making

Designers are confronted with a formidable challenge when making decisions about design options from the array of solutions proposed by the Pareto fronts. MCDM techniques such as TOPSIS and VIKOR can effectively address this issue. These procedures rely on an aggregation approach that assesses the proximity to the ideal point. Nevertheless, there is a differentiation between these techniques concerning their normalization processes. VIKOR implements linear normalization for the objectives, whereas TOPSIS employs Euclidean normalization. Numerous sources [96–99] have extensively investigated and documented the effectiveness of both approaches through comprehensive research studies.

7.1. TOPSIS approach

The TOPSIS method utilizes a sequential process for ranking alternatives, which includes the following steps.

1. Forming the decision-making matrix (DMM): $(x_{ij})_{m\times n}$.
2. Normalizing DMM using the Euclidean approach:

$$R=(r_{ij})_{m\times n}, r_{ij}=\frac{x_{ij}}{\sqrt{\sum_{k=1}^{m}x_{kj}^2}} \quad i=1,2,\ldots,m \quad j=1,2,\ldots,n \tag{42}$$

3. Weighting to the DMM:

$$S_{ij}=r_{ij}\bullet w_j, i=1,2,\ldots,m \quad j=1,2,\ldots,n \tag{43}$$

4. Identifying the best and worst alternatives:

$$A_{best}=\left\{\langle min\left(t_{ij}\middle|i=1,2,\ldots,m\right)\middle|j\in J_-\rangle,\langle max\left(t_{ij}\middle|i=1,2,\ldots,m\right)\middle|j\in J_+\rangle\right\} \equiv\left\{t_{bj}\middle|j=1,2,\ldots,n\right\} \tag{44}$$

$$A_{worst}=\left\{\langle max\left(t_{ij}\middle|i=1,2,\ldots,m\right)\middle|j\in J_-\rangle,\langle min\left(t_{ij}\middle|i=1,2,\ldots,m\right)\middle|j\in J_+\rangle\right\} \equiv\left\{t_{wj}\middle|j=1,2,\ldots,n\right\} \tag{45}$$

where

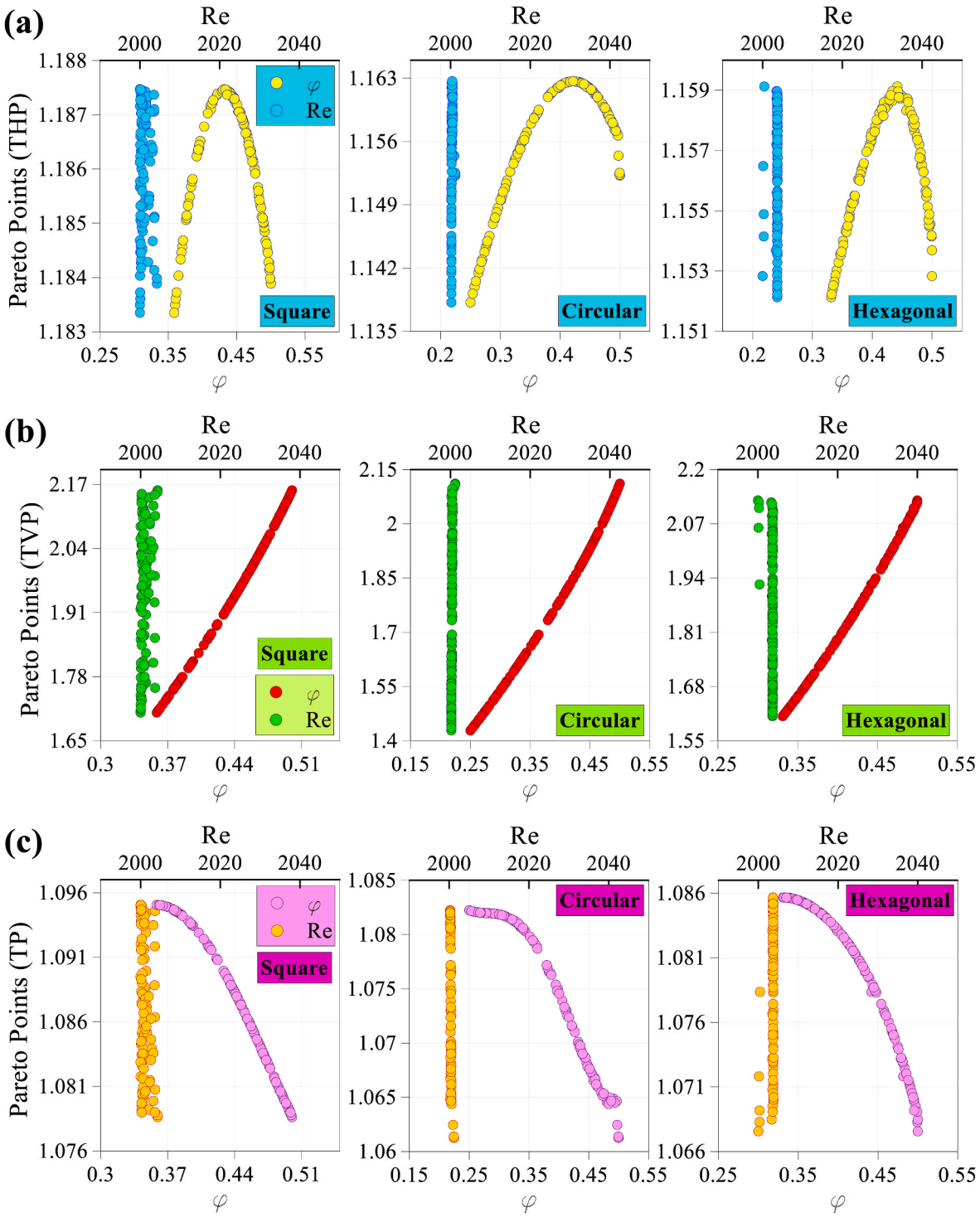

Fig. 13. Distribution of optimal points of (a) THP, (b) TVP, and (c) TP for various values of Re, PS and φ.

$$J_+ = \{j = 1, 2, \ldots, n | j\}, J_- = \{j = 1, 2, \ldots, n | j\} \quad (46)$$

J_+ and J_- represent the criteria with positive and negative impacts.

5. Calculating each alternative's Euclidean distance according to the worst and best solution.

$$D_{i,worst} = \sqrt{\sum_{j=1}^{n} \left(t_{ij} - t_{wj}\right)^2}, D_{i,best} = \sqrt{\sum_{j=1}^{n} \left(t_{ij} - t_{bj}\right)^2}, i = 1, 2, \ldots, m \quad (47)$$

6. Ranking alternatives:

$$S_{i,worst} = \frac{D_{i,worst}}{D_{i,best} + D_{i,worst}}, 0 \le S_{i,worst} \le 1, i = 1, 2, \ldots, m \quad (48)$$

The TOPSIS determines the best alternative by selecting the design point with the highest $S_{i,worst}$ value.

7.2. VIKOR approach

The VIKOR method employs a sequential process for ranking alternatives, which consists of the following steps.

1. Creating DMM ($(x_{ij})_{m\times n}$) similar to the TOPSIS.
2. Identifying the best and worst alternatives:

When j-th criterion is positive:

$$f_j^* = max\left[\left(x_{ij}\right)\middle| i=1,2,\ldots,m\right], j=1,2,\ldots,n \tag{49}$$

$$f_j^- = min\left[\left(x_{ij}\right)\middle| i=1,2,\ldots,m\right], j=1,2,\ldots,n \tag{50}$$

When j-th criterion is negative:

$$f_j^* = min\left[\left(x_{ij}\right)\middle| i=1,2,\ldots,m\right], j=1,2,\ldots,n \tag{51}$$

$$f_j^- = max\left[\left(x_{ij}\right)\middle| i=1,2,\ldots,m\right], j=1,2,\ldots,n \tag{52}$$

3. Weighting criteria by defining two parameters of utility measure (S_i) and regret measure (R_i):

$$R_i = max\left[w_j \bullet \frac{f_j^* - x_{ij}}{f_j^* - f_j^-}\right], j=1,2,\ldots,n, i=1,2,\ldots,m \tag{53}$$

$$S_i = \sum_{j=1}^{n} w_j \bullet \frac{f_j^* - x_{ij}}{f_j^* - f_j^-}, j=1,2,\ldots,n, i=1,2,\ldots,m \tag{54}$$

4. Ranking alternatives using VIKOR index (Q_i):

5. $$Q_i = v \bullet \frac{S_i - S^*}{S^- - S^*} + (1-v) \bullet \frac{R_i - R^*}{R^- - R^*}, i=1,2,\ldots,m \tag{55}$$

where

$$S^* = min[S_i|i=1,2,\ldots,m], S^- = max[S_i|i=1,2,\ldots,m] \tag{56}$$

$$R^* = min[S_i|i=1,2,\ldots,m], \quad R^- = max[S_i|i=1,2,\ldots,m] \tag{57}$$

In order to create a procedure that balances utility and regret criteria, the value of v is set to 0.5. The superior alternative is determined by identifying the alternative with the lowest VIKOR index.

7.3. MCDM-based desirable points

While a changeover in the Pareto front points does cause a shift in the design variables and objective values, it does not necessarily result in an enhanced design point. Therefore, moving from one point to another on the Pareto front changes the relative importance of the objectives. In such a scenario, when faced with multiple available solutions, the designer must make a principled decision using MCDM techniques. MCDM approaches help the designer choose the desirable optimal points by assigning weight or importance coefficients to different objectives.

Table 10 presents the single-objective and MCDM-based desirable points for different weights of objectives. In addition, the optimal points presented in Table 10 are shown graphically on the Pareto fronts in Fig. 14. Table 10 clearly reveals that all the proposed design points have square perforations and Reynolds numbers around 2000 regardless of whether the decision-making is based on one, two or three objectives. From this initial analysis, it can be inferred that the perforations' size (φ) is the sole design variable influencing the distinction between various DM-based designs.

The importance of considering the single-objective design of the current PFHS should not be underestimated. Indeed, each individual redefined objective holds substantial importance as a criterion in the design of each heat sink. As an illustration, in the single-objective design of PFHS utilizing THP, both the HTR and pressure drop are simultaneously considered, which is acceptable to be adequate in numerous practical applications. Moreover, with the TVP-based single-objective design of PFHS, it becomes possible to optimize both the HTR and the volume of the heat sink. Also, in many practical applications where heat dissipation is the main priority, the TP-based single-objective design is accomplished without considering the heat sink volume and pressure drop.

Point A is the optimal solution for THP-based single-objective design. The value of φ at this point is equal to 0.43, which achieves the optimal balance between increasing heat transfer and decreasing pressure drop with large-size perforations. Considering the single-objective design based on TVP (point B), the optimal design includes the largest possible size for perforations ($\varphi = 0.5$). This design offers the lightest heat sink with acceptable thermal performance. On the other hand, a single-objective design based on TP (point C) suggests a desirable design with $\varphi = 0.36$. This intermediate φ-value indicates the maximization of thermal performance in the average perforations' size.

Point D shows the two-criteria decision-making based on THP and TVP with TOPSIS and VIKOR methods, which leads to φ-values of 0.5 and 0.494, respectively. Both MCDM techniques suggest the optimal points for the design, which have the largest perforations' volume. This

Table 10
Single-Objective and MCDM-based desirable points for different weights of objectives.

DM methods		Points	Weight			Input variables			Objectives		
			THP	TVP	TP	φ	Re	PS	THP	TVP	TP
Single-Objective		**A**	1	0	0	0.4318	2000	square	1.1875	1.9171	1.0895
		B	0	1	0	0.5	2004.3	square	1.1839	2.1580	1.0786
		C	0	0	1	0.3586	2000	square	1.1834	1.7070	1.0951
TOPSIS	**Two-Objectives**	$\mathbf{D_T}$	1	1	0	0.5	2004.3	square	1.1839	2.1580	1.0786
		$\mathbf{E_T}$	1	0	1	0.3915	2000.1	square	1.1862	1.7971	1.0938
		$\mathbf{F_T}$	0	1	1	0.5	2004.3	square	1.1839	2.1580	1.0786
	Three-Objectives	$\mathbf{G_T}$	1	1	1	0.5	2004.3	square	1.1839	2.1580	1.0786
		$\mathbf{H_T}$	3	1	1	0.4984	2000.3	square	1.1842	2.1507	1.0790
		$\mathbf{I_T}$	1	3	1	0.5	2004.3	square	1.1839	2.1580	1.0786
		$\mathbf{J_T}$	1	1	3	0.4984	2000.3	square	1.1842	2.1507	1.0790
VIKOR	**Two-Objectives**	$\mathbf{D_V}$	1	1	0	0.4937	2000.2	square	1.1846	2.1324	1.0797
		$\mathbf{E_V}$	1	0	1	0.3855	2001.0	square	1.1858	1.7797	1.0942
		$\mathbf{F_V}$	0	1	1	0.4507	2000.7	square	1.1872	1.9777	1.0867
	Three-Objectives	$\mathbf{G_V}$	1	1	1	0.4507	2000.7	square	1.1872	1.9777	1.0867
		$\mathbf{H_V}$	3	1	1	0.4507	2000.7	square	1.1872	1.9777	1.0867
		$\mathbf{I_V}$	1	3	1	0.4984	2000.3	square	1.1842	2.1507	1.0790
		$\mathbf{J_V}$	1	1	3	0.4115	2000.0	square	1.1872	1.8551	1.0920

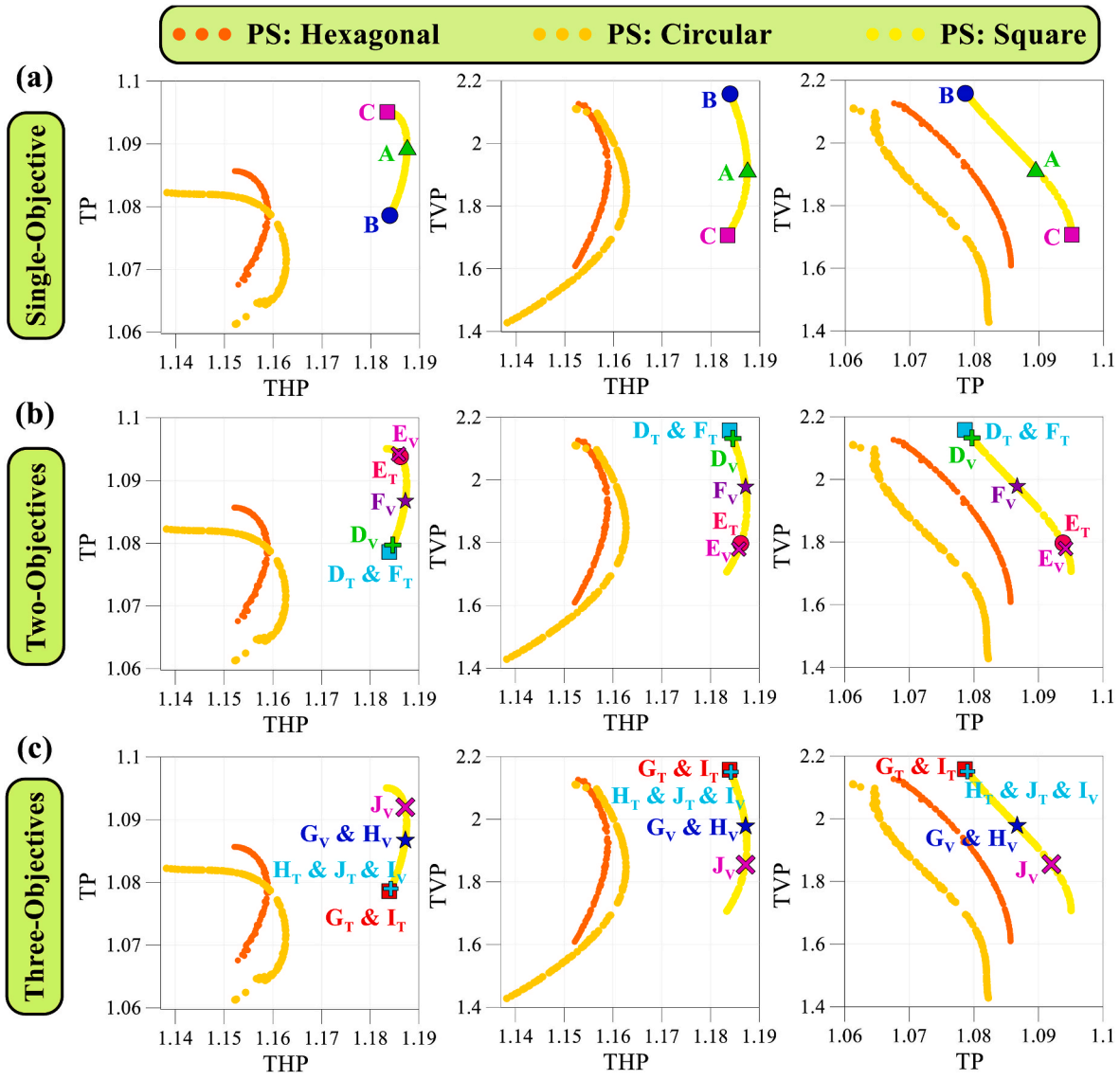

Fig. 14. Single-Objective and MCDM-based desirable points on the Pareto fronts.

high volume leads to an increase in hydraulic and weight efficiency. Point E makes the two objectives of THP and TP the basis for decision-making. Both TOPSIS and VIKOR methods suggest a φ-value of about 0.39, which has a satisfactory hydraulically and thermally effective balance. At point F, which considers the importance of TVP and TP, the perforations volume ratio for the proposed TOPSIS technique ($\varphi = 0.5$) is higher than that of VIKOR ($\varphi = 0.45$).

Three-criteria decision-making is implemented in four different scenarios. In the first scenario, each objective is given equal weight ($W_{THP} = W_{TVP} = W_{TP} = 1$). In the other three scenarios, the weight of each objective is three times the other two objectives. Point G describes a scenario where all three objectives have equal weight. In this case, the TOPSIS method ($\varphi = 0.5$) finds a larger perforations' volume than the VIKOR method ($\varphi = 0.45$). This trend can be seen in three other scenarios. At point H, where THP has more weight than the other two objectives, the TOPSIS ($\varphi = 0.4984$) recognizes that the perforations' volume close to the maximum is desirable. At the same time, VIKOR ($\varphi = 0.4507$) suggests a smaller value than the TOPSIS. Also, at point I, where TVP becomes very important, the TOPSIS method ($\varphi = 0.5$) and VIKOR ($\varphi = 0.4984$) recommend the maximum possible volume for perforations. Finally, by assigning an importance coefficient of three to the TP, point J highlights a significant difference in the perforations volume ratio between the PFHS proposed by TOPSIS ($\varphi = 0.4984$) and VIKOR ($\varphi = 0.4115$).

8. Conclusion

Designing high-efficiency heat sinks presents a considerable challenge in thermo-fluid engineering. Using longitudinal and lateral perforations is an exceptionally effective and innovative approach to optimizing heat sinks for diverse equipment applications. Implementing this approach results in the simultaneous enhancement of heat dissipation, pressure drop, and weight of heat sinks, which are essential objectives that designers must consider when designing heat sinks. To highlight the significance of the optimized design of PFHSs, the present authors have introduced a novel hybrid strategy that combines computational fluid dynamics, machine learning, multi-objective optimization, and multi-criteria decision-making. The primary objective of the present study is to offer adaptable and optimized solutions with respect to the significance of various objectives. The geometric design variables encompass the size and shape of the perforations, whereas the Reynolds number is an input variable that pertains to the fluid flow. The design objectives are reformulated as dimensionless representations of heat dissipation, pressure drop, and heat sink weight. These revised

objectives contain thermal performance, thermo-hydraulic performance, and thermo-volumetric performance. The groundbreaking design process employed in the present investigation has the potential to not only revolutionize the design of heat sinks but also transform various engineering and industrial phenomena.

The key discoveries of this research can be summarized as follows.

- Both stepwise mixed selection (SMS) and GMDH-NN techniques exhibited comparable performance in most modeling scenarios. Nevertheless, the SMS approach demonstrated more reliability in modeling diverse objectives.
- The SMS method outperformed the GMDH-NN technique in predicting THP, achieving R-values of 0.999743, 0.997620, and 0.996580 for PFHS with square, circular, and hexagonal cross-sectional perforations, respectively.
- The TVP models based on the SMS method indicated the most reliable correlation coefficient values of 0.999996 and 0.999934 for PFHS with square and circular perforations, respectively. The superiority of GMDH-based models compared to SMS models was evident for hexagonal-based PFHSs with R = 0.999966.
- The SMS method in the TP modeling process yielded the highest R-values of 0.999592 and 0.992566 for square and circular cross-sectional perforations. In contrast, GMDH-NN (R = 0.998058) performed better than SMS for PFHSs with hexagonal perforations.
- The optimization results showed that the optimal size of the perforations is strongly dependent on their shapes. For example, in PFHSs with square perforations, approximately 54% of the Pareto points had a φ-value greater than 0.45. While in PFHSs based on circular perforations, more than 50% of the optimal points have φ less than 0.4.
- By exploring different weighting scenarios in the MCDM process, PFHSs with square perforations and Reynolds numbers of approximately 2000 across a wide range of perforations' sizes could lead to optimal designs.

In future studies, the proposed hybrid method can be extended to optimize perforated fins in heat sinks with different types of fin geometries, including radial, annular, and pin-shaped fins. Furthermore, by applying the proposed method to a wide range of constant Reynolds numbers, valuable insights can be gained regarding optimal configurations under varying fluid velocities.

CRediT authorship contribution statement

Seyyed Amirreza Abdollahi: Conceptualization, Formal analysis, Software, Writing – original draft. **Ali Basem:** Formal analysis, Visualization, Writing – original draft. **As'ad Alizadeh:** Methodology, Supervision, Writing – original draft. **Dheyaa J. Jasim:** Data curation, Formal analysis, Software. **Mohsen Ahmed:** Formal analysis, Resources, Validation, Writing – review & editing. **Abbas J. Sultan:** Data curation, Formal analysis, Resources, Writing – review & editing. **Seyyed Faramarz Ranjbar:** Investigation, Methodology, Writing – review & editing. **Hamid Maleki:** Data curation, Formal analysis, Software, Writing – original draft.

Declaration of competing interest

The authors declare that they have no known competing financial interests or personal relationships that could have appeared to influence the work reported in this paper.

Data availability

Data will be made available on request.

Nomenclature

ΔA	area (m^2)
C_p	specific heat at constant pressure (J kg^{-1} K^{-1})
D	fin thickness (m)
F_F	friction drag (N)
F_P	pressure drag (N)
F_T	total drag (N)
h	heat transfer coefficient (W m^{-2} K^{-1})
H	fin height (m)
k	turbulent kinetic energy (m^2 s^{-2})
L	fin length (m)
Nu	Nusselt number (-)
P	fluid pressure (Pa)
q	the heat transfer rate (W)
R_{th}	thermal resistance (K W^{-1})
Re	Reynolds number (-)
T	temperature (K)
u	velocity component in the X direction (m s^{-1})
v	velocity component in the Y direction (m s^{-1})
w	velocity component in the Z direction (m s^{-1})
W	weight of fin (kg)
V	fin volume (m^3)
X,Y,Z	rectangular coordinates (m)

Subscripts

b	fin base
eff	effective
DS	downstream
in	inlet
pf	perforated fin

s	the surface of the fin
sf	solid fin
US	upstream
∞	free stream

Greek symbols

ε	turbulent dissipation rate ($m^2\ s^{-3}$)
μ	fluid viscosity ($kg\ m^{-1}\ s^{-1}$)
μ_t	turbulent viscosity ($kg\ m^{-1}\ s^{-1}$)
ρ	fluid density ($kg\ m^{-3}$)
λ	Thermal conductivity of fluid ($W\ m^{-1}\ K^{-1}$)
λ_t	turbulent thermal conductivity of fluid ($W\ m^{-1}\ K^{-1}$)
σ	Heat transfer surface ratio (-)
τ_w	wall shear stress (Pa)
φ	Perforations volume ratio (-)

Abbreviations

ADC	Average Drag Coefficient
AI	Artificial Intelligence
ANN	Artificial Neural Network
ANuN	Average Nusselt Number
CFD	Computational Fluid Dynamics
COMBI	Combinatorial algorithm
FVM	Finite Volume Method
GMDH	Group Method of Data Handling
HTE	Heat Transfer Enhancement
HTR	Heat Transfer Rate
MAPE	Mean Absolute Percentage Error
MCDM	Multi-Criteria Decision-Making
ML	Machine Learning
MOO	Multi-objective Optimization
NSGA-II	Non-Dominated Sorting Genetic Algorithm II
PFHS	Perforated Finned Heat Sink
PS	Perorations Shape
RMSE	Root Mean Square Error
SFHS	Solid Finned Heat Sink
THP	Thermo-hydraulic Performance
TP	Thermal Performance
TVP	Thermo-volumetric Performance

References

[1] S. Thapa, S. Samir, K. Kumar, S. Singh, A review study on the active methods of heat transfer enhancement in heat exchangers using electroactive and magnetic materials, Mater. Today: Proc. 45 (2021) 4942–4947.

[2] M.H. Mousa, N. Miljkovic, K. Nawaz, Review of heat transfer enhancement techniques for single phase flows, Renew. Sustain. Energy Rev. 137 (2021) 110566.

[3] J. Tang, X. Hu, Y. Yu, Electric field effect on the heat transfer enhancement in a vertical rectangular microgrooves heat sink, Int. J. Therm. Sci. 150 (2020) 106222.

[4] S. Giwa, M. Sharifpur, M. Ahmadi, J. Meyer, A review of magnetic field influence on natural convection heat transfer performance of nanofluids in square cavities, J. Therm. Anal. Calorim. 145 (5) (2021) 2581–2623.

[5] W.L. Staats, J.G. Brisson, Active heat transfer enhancement in air cooled heat sinks using integrated centrifugal fans, Int. J. Heat Mass Tran. 82 (2015) 189–205.

[6] T. Gan, et al., Heat transfer enhancement of a microchannel heat sink with the combination of impinging jets, dimples, and side outlets, J. Therm. Anal. Calorim. 141 (1) (2020) 45–56.

[7] A. Hosseinian, A.M. Isfahani, E. Shirani, Experimental investigation of surface vibration effects on increasing the stability and heat transfer coeffcient of MWCNTs-water nanofluid in a flexible double pipe heat exchanger, Exp. Therm. Fluid Sci. 90 (2018) 275–285.

[8] M. Setareh, M. Saffar-Avval, A. Abdullah, Experimental and numerical study on heat transfer enhancement using ultrasonic vibration in a double-pipe heat exchanger, Appl. Therm. Eng. 159 (2019) 113867.

[9] M. Habibishandiz, M. Saghir, A critical review of heat transfer enhancement methods in the presence of porous media, nanofluids, and microorganisms, Therm. Sci. Eng. Prog. 30 (2022) 101267.

[10] M. Hajmohammadi, H. Maleki, G. Lorenzini, S. Nourazar, Effects of Cu and Ag nano-particles on flow and heat transfer from permeable surfaces, Adv. Powder Technol. 26 (1) (2015) 193–199.

[11] H. Maleki, J. Alsarraf, A. Moghanizadeh, H. Hajabdollahi, M.R. Safaei, Heat transfer and nanofluid flow over a porous plate with radiation and slip boundary conditions, J. Cent. S. Univ. 26 (5) (2019) 1099–1115.

[12] H. Maleki, M.R. Safaei, A.A. Alrashed, A. Kasaeian, Flow and heat transfer in non-Newtonian nanofluids over porous surfaces, J. Therm. Anal. Calorim. 135 (3) (2019) 1655–1666.

[13] H. Maleki, M.R. Safaei, H. Togun, M. Dahari, Heat transfer and fluid flow of pseudo-plastic nanofluid over a moving permeable plate with viscous dissipation and heat absorption/generation, J. Therm. Anal. Calorim. 135 (3) (2019) 1643–1654.

[14] H. Maleki, M. Zolfaghar, M. Mohseni, Effects of suction/injection on flow and heat transfer over a permeable surface in presence of different nanofluids, Modares Mechanical Engineering 17 (9) (2017) 439–449.

[15] D.J. Jasim, et al., Evaluation of different methods to ameliorate the performance of PV/T systems using hybrid nanofluids and PCM in a spiral tube with different cross sections, Results in Engineering 20 (2023) 101514.

[16] M.J. Hasan, S.F. Ahmed, A.A. Bhuiyan, Geometrical and coil revolution effects on the performance enhancement of a helical heat exchanger using nanofluids, Case Stud. Therm. Eng. 35 (2022) 102106.

[17] M.J. Hasan, A.A. Bhuiyan, Investigation of thermal performance and entropy generation in a helical heat exchanger with multiple rib profiles using Al2O3-water nanofluid, Case Stud. Therm. Eng. 40 (2022) 102514.

[18] M.J. Hasan, A.A. Bhuiyan, Thermo-hydrodynamic characteristics and entropy generation in a tube heat exchanger using multiple head ribbed geometries, S. Afr. J. Chem. Eng. 45 (2023) 305–314.

[19] M.K. Fahad, N.F. Ifraj, S.H. Tahsin, M.J. Hasan, Numerical investigation of the hydrothermal performance of novel vortex generators in a rectangular channel by employing inclination and rotational angles, International Journal of Thermofluids 20 (2023) 100500.

[20] S.D. Shelare, K.R. Aglawe, P.N. Belkhode, A review on twisted tape inserts for enhancing the heat transfer, Mater. Today: Proc. 54 (2022) 560–565.

[21] B. Sterr, E. Mahravan, D. Kim, Uncertainty quantification of heat transfer in a microchannel heat sink with random surface roughness, Int. J. Heat Mass Tran. 174 (2021) 121307.
[22] H. Alimoradi, M. Shams, N. Ashgriz, A. Bozorgnezhad, A novel scheme for simulating the effect of microstructure surface roughness on the heat transfer characteristics of subcooled flow boiling, Case Stud. Therm. Eng. 24 (2021) 100829.
[23] H. Maleki, M.R. Safaei, A.S. Leon, T.K. Nguyen, Thermal and hydraulic performance of longitudinal perforated rectangular fins with perforation shape and size variations, in: ASTFE Digital Library, Begel House Inc, 2019.
[24] Y. Zhou, et al., Computational fluid dynamics and multi-objective response surface methodology optimization of perforated-finned heat sinks, J. Taiwan Inst. Chem. Eng. 145 (2023) 104823.
[25] H. Maleki, M. Ashrafi, N.Z. Ilghani, M. Goodarzi, T. Muhammad, Pareto optimal design of a finned latent heat thermal energy storage unit using a novel hybrid technique, J. Energy Storage 44 (2021) 103310.
[26] F.B. Majmader, M.J. Hasan, Thermal enhancement and entropy generation of an air-cooled 3D radiator with modified fin geometry and perforation: a numerical study, Case Stud. Therm. Eng. 52 (2023) 103671.
[27] M.O. Qidwai, M.M. Hasan, N.Z. Khan, U. Khan, Optimization of heat transfer effects in radial fin microchannel heat sink. Energy Sources, Part A: Recovery, Utilization, and Environmental Effects, 2019, pp. 1–13.
[28] M. Hajmohammadi, E. Rasouli, M.A. Elmi, Geometric optimization of a highly conductive insert intruding an annular fin, Int. J. Heat Mass Tran. 146 (2020) 118910.
[29] H. Maleki, M.R. Safaei, A.S. Leon, T. Muhammad, T.K. Nguyen, Improving shipboard electronics cooling system by optimizing the heat sinks configuration, J. Ocean Eng. Sci. 7 (2022) 498–508.
[30] H.A. Hussein, Numerical hydrothermal evaluation of heat transfer in a multi-mini-channel heat sink: effect of square pin fins. Results in Engineering, 2023 101403.
[31] J. Li, et al., Multi-objective optimization of a laterally perforated-finned heat sink with computational fluid dynamics method and statistical modeling using response surface methodology, Eng. Appl. Artif. Intell. 130 (2024) 107674.
[32] F.N. Ghadhban, H.M. Jaffal, Numerical investigation on heat transfer and fluid flow in a multi-minichannel heat sink: effect of channel configurations, Results in Engineering 17 (2023) 100839.
[33] R. Adhikari, D. Wood, M. Pahlevani, Optimizing rectangular fins for natural convection cooling using CFD, Therm. Sci. Eng. Prog. 17 (2020) 100484.
[34] M. Rabani, M. Rabani, Heating performance enhancement of a new design trombe wall using rectangular thermal fin arrays: an experimental approach, J. Energy Storage 24 (2019) 100796.
[35] A. Sathe, S. Sanap, S. Dingare, N. Sane, Investigation of thermal performance of modified vertical rectangular fin array in free convection using experimental and numerical method, Mater. Today: Proc. 38 (2021) 2281–2290.
[36] R. Cong, Y. Ozaki, B.S. Machado, P.K. Das, Constructal design of a rectangular fin in a mixed convective confined environment, Inventions 3 (2) (2018) 27.
[37] A. Dasore, et al., Comparative numerical investigation of rectangular and elliptical fins for air cooled IC engines, Mater. Today: Proc. 49 (2022) 481–485.
[38] V. Karlapalem, S.K. Dash, Design of perforated branching fins in laminar natural convection, Int. Commun. Heat Mass Tran. 120 (2021) 105071.
[39] S.V. Hudișteanu, F.E. Țurcanu, N.C. Cherecheș, C.G. Popovici, M. Verdeș, I. Huditeanu, Enhancement of PV panel power production by passive cooling using heat sinks with perforated fins, Appl. Sci. 11 (23) (2021) 11323.
[40] K. Egab, S.K. Oudah, Thermal management analysis of li-ion battery-based on cooling system using dimples with air fins and perforated fins, Int. J. Therm. Sci. 171 (2022) 107200.
[41] S. Chingulpitak, H.S. Ahn, L.G. Asirvatham, S. Wongwises, Fluid flow and heat transfer characteristics of heat sinks with laterally perforated plate fins, Int. J. Heat Mass Tran. 138 (2019) 293–303.
[42] M. Shaeri, M. Yaghoubi, Thermal enhancement from heat sinks by using perforated fins, Energy Convers. Manag. 50 (5) (2009) 1264–1270.
[43] M. Shaeri, M. Yaghoubi, Numerical analysis of turbulent convection heat transfer from an array of perforated fins, Int. J. Heat Fluid Flow 30 (2) (2009) 218–228.
[44] M.R. Shaeri, T.-C. Jen, Turbulent heat transfer analysis of a three-dimensional array of perforated fins due to changes in perforation sizes, Numer. Heat Tran., Part A: Applications 61 (11) (2012) 807–822.
[45] M. Shaeri, M. Yaghoubi, K. Jafarpur, Heat transfer analysis of lateral perforated fin heat sinks, Appl. Energy 86 (10) (2009) 2019–2029.
[46] M.R. Shaeri, R. Bonner, Heat transfer and pressure drop in laterally perforated-finned heat sinks across different flow regimes, Int. Commun. Heat Mass Tran. 87 (2017) 220–227.
[47] M.R. Shaeri, R.W. Bonner III, Analytical heat transfer model for laterally perforated-finned heat sinks, Int. J. Heat Mass Tran. 131 (2019) 1164–1173.
[48] A.M. Roy, Adaptive transfer learning-based multiscale feature fused deep convolutional neural network for EEG MI multiclassification in brain–computer interface, Eng. Appl. Artif. Intell. 116 (2022) 105347.
[49] M. Sepehrnia, H. Maleki, M. Karimi, E. Nabati, Examining rheological behavior of CeO2-GO-SA/10W40 ternary hybrid nanofluid based on experiments and COMBI/ANN/RSM modeling, Sci. Rep. 12 (1) (2022) 1–22.
[50] H. Fattahi, N. Zandy Ilghani, Application of Monte Carlo Markov chain and GMDH neural network for estimating the behavior of suction caissons in clay, Geotech. Geol. Eng. (2023) 1–15.
[51] H. Fattahi, N. Zandy Ilghani, Hybrid wavelet transform with artificial neural network for forecasting of shear wave velocity from wireline log data: a case study, Environ. Earth Sci. 80 (2021) 1–10.
[52] R. Langbauer, G. Nunner, T. Zmek, J. Klarner, R. Prieler, C. Hochenauer, Modelling of thermal shrinkage of seamless steel pipes using artificial neural networks (ANN) focussing on the influence of the ANN architecture, Results in Engineering 17 (2023) 100999.
[53] P. Zafari, A. Ghaemi, Modeling and optimization of CO2 capture into mixed MEA-PZ amine solutions using machine learning based on ANN and RSM models, Results in Engineering 19 (2023) 101279.
[54] A. Shahsavar, M. Sepehrnia, H. Maleki, R. Darabi, Thermal conductivity of hydraulic oil-GO/Fe3O4/TiO2 ternary hybrid nanofluid: experimental study, RSM analysis, and development of optimized GPR model, J. Mol. Liq. (2023) 122338.
[55] J. Zhou, et al., Optimization of support vector machine through the use of metaheuristic algorithms in forecasting TBM advance rate, Eng. Appl. Artif. Intell. 97 (2021) 104015.
[56] N. Qian, X. Wang, Y. Fu, Z. Zhao, J. Xu, J. Chen, Predicting heat transfer of oscillating heat pipes for machining processes based on extreme gradient boosting algorithm, Appl. Therm. Eng. 164 (2020) 114521.
[57] H. Wang, C. Ji, J. Yang, S. Wang, Y. Ge, Towards a comprehensive optimization of the intake characteristics for side ported Wankel rotary engines by coupling machine learning with genetic algorithm, Energy 261 (2022) 125334.
[58] H. Wang, et al., Multi-objective optimization of a hydrogen-fueled Wankel rotary engine based on machine learning and genetic algorithm, Energy 263 (2023) 125961.
[59] A.H. Elsheikh, Applications of machine learning in friction stir welding: prediction of joint properties, real-time control and tool failure diagnosis, Eng. Appl. Artif. Intell. 121 (2023) 105961.
[60] G. Krishnayatra, S. Tokas, R. Kumar, Numerical heat transfer analysis & predicting thermal performance of fins for a novel heat exchanger using machine learning, Case Stud. Therm. Eng. 21 (2020) 100706.
[61] L.F. Sepulveda, et al., Forecasting of individual electricity consumption using optimized gradient boosting regression with modified particle swarm optimization, Eng. Appl. Artif. Intell. 105 (2021) 104440.
[62] H. Fattahi, M. Hasanipanah, N. Zandy Ilghani, Investigating correlation of physico-mechanical parameters and P-wave velocity of rocks: a comparative intelligent study, Journal of Mining and Environment 12 (3) (2021) 863–875.
[63] A. Dezhkam, M.T. Manzuri, Forecasting stock market for an efficient portfolio by combining XGBoost and Hilbert–Huang transform, Eng. Appl. Artif. Intell. 118 (2023) 105626.
[64] M. Sepehrnia, H. Maleki, M.F. Behbahani, Tribological and Rheological Properties of Novel MoO3-GO-MWCNTs/5W30 Ternary Hybrid Nanolubricant: Experimental Measurement, Development of Practical Correlation, and Artificial Intelligence Modeling, Powder Technology, 2023 118389.
[65] M. Sepehrnia, A. Shahsavar, H. Maleki, A. Moradi, Experimental study on the dynamic viscosity of hydraulic oil HLP 68-Fe3O4-TiO2-GO ternary hybrid nanofluid and modeling utilizing machine learning technique, J. Taiwan Inst. Chem. Eng. 145 (2023) 104841.
[66] F.E. Jalal, Y. Xu, M. Iqbal, M.F. Javed, B. Jamhiri, Predictive modeling of swell-strength of expansive soils using artificial intelligence approaches: ANN, ANFIS and GEP, J. Environ. Manag. 289 (2021) 112420.
[67] Z. Zhang, et al., Optimized ANFIS models based on grid partitioning, subtractive clustering, and fuzzy C-means to precise prediction of thermophysical properties of hybrid nanofluids, Chem. Eng. J. (2023) 144362.
[68] Q. Wang, S. Zhang, Y. Zhang, J. Fu, Z. Liu, Enhancing performance of nanofluid mini-channel heat sinks through machine learning and multi-objective optimization of operating parameters, Int. J. Heat Mass Tran. 210 (2023) 124204.
[69] M. Saeed, R.S. Kalule, A.S. Berrouk, M. Alshehhi, E. Almatrafi, Machine learning-based optimization of a mini-channel heatsink geometry, Arabian J. Sci. Eng. (2023) 1–18.
[70] A. Tikadar, S. Kumar, Investigation of thermal-hydraulic performance of metal-foam heat sink using machine learning approach, Int. J. Heat Mass Tran. 199 (2022) 123438.
[71] A. Sikirica, L. Grbčić, L. Kranjčević, Machine learning based surrogate models for microchannel heat sink optimization, Appl. Therm. Eng. 222 (2023) 119917.
[72] M.R. Shaeri, S. Sarabi, A.M. Randriambololona, A. Shadlo, Machine learning-based optimization of air-cooled heat sinks, Therm. Sci. Eng. Prog. 34 (2022) 101398.
[73] K. Kim, et al., A machine learning approach for predicting heat transfer characteristics in micro-pin fin heat sinks, Int. J. Heat Mass Tran. 194 (2022) 123087.
[74] J. Mohammadpour, S. Husain, F. Salehi, A. Lee, Machine learning regression-CFD models for the nanofluid heat transfer of a microchannel heat sink with double synthetic jets, Int. Commun. Heat Mass Tran. 130 (2022) 105808.
[75] A. Suzuki, H. Nakatani, M. Kobashi, Machine learning surrogate modeling toward the design of lattice-structured heat sinks fabricated by additive manufacturing, Mater. Des. 230 (2023) 111969.
[76] S.-H. Ahn, Y. Xiao, Z. Wang, Y. Luo, H. Fan, Unsteady prediction of cavitating flow around a three dimensional hydrofoil by using a modified RNG k-ε model, Ocean. Eng. 158 (2018) 275–285.
[77] E. Velayati, M. Yaghoubi, Numerical study of convective heat transfer from an array of parallel bluff plates, Int. J. Heat Fluid Flow 26 (1) (2005) 80–91.
[78] M.H. Zaidan, A.A. Alkumait, T.K. Ibrahim, Assessment of heat transfer and fluid flow characteristics within finned flat tube, Case Stud. Therm. Eng. 12 (2018) 557–562.
[79] H. Singh, S. Chavadaki, C. Kishore, K.N. Kumar, S. Avikal, Numerical analysis of roughened solar air heater with arc and fan shape roughness to understand heat transfer and fluid flow characteristics, Mater. Today: Proc. 46 (2021) 10662–10667.

[80] A.K. Hilo, Fluid flow and heat transfer over corrugated backward facing step channel, Case Stud. Therm. Eng. 24 (2021) 100862.
[81] V. Yakhot, S. Orszag, S. Thangam, T. Gatski, C. Speziale, Development of turbulence models for shear flows by a double expansion technique, Phys. Fluid. Fluid Dynam. 4 (7) (1992) 1510–1520.
[82] S.V. Patankar, Numerical Heat Transfer and Fluid Flow, CRC press, 2018.
[83] H. Jonsson, B. Moshfegh, Modeling of the thermal and hydraulic performance of plate fin, strip fin, and pin fin heat sinks-influence of flow bypass, IEEE Trans. Compon. Packag. Technol. 24 (2) (2001) 142–149.
[84] F.J. Gravetter, L.B. Wallnau, L.-A.B. Forzano, J.E. Witnauer, Essentials of Statistics for the Behavioral Sciences, Cengage Learning, 2020.
[85] A. Desgagné, P. Lafaye de Micheaux, A powerful and interpretable alternative to the Jarque–Bera test of normality based on 2nd-power skewness and kurtosis, using the Rao's score test on the APD family, J. Appl. Stat. 45 (13) (2018) 2307–2327.
[86] F. Andy, Discovering Statistics Using SPSS, 2009.
[87] S.-D. Bolboaca, L. Jäntschi, Pearson versus Spearman, Kendall's tau correlation analysis on structure-activity relationships of biologic active compounds, Leonardo J. Sci. 5 (9) (2006) 179–200.
[88] A. Shirbazo, M. Keshavarz Moraveji, A new pressure and temperature dependent relative viscosity model for water-Al2O3 nanofluids using GMDH neural network, Petrol. Sci. Technol. (2022) 1–21.
[89] A.G. Ivakhnenko, Polynomial theory of complex systems, IEEE transactions on Systems, Man, and Cybernetics 4 (1971) 364–378.
[90] T. Zhang, et al., Optimization of thermophysical properties of nanofluids using a hybrid procedure based on machine learning, multi-objective optimization, and multi-criteria decision-making, Chem. Eng. J. 485 (2024) 150059.
[91] S.J. Farlow, Self-organizing Methods in Modeling: GMDH Type Algorithms, CrC Press, 2020.
[92] N. Nikolaev, H. Iba, Adaptive Learning of Polynomial Networks: Genetic Programming, Backpropagation and Bayesian Methods, Springer Science & Business Media, 2006.
[93] C.J. Willmott, Some comments on the evaluation of model performance, Bull. Am. Meteorol. Soc. 63 (11) (1982) 1309–1313.
[94] H. Pham, A new criterion for model selection, Mathematics 7 (12) (2019) 1215.
[95] K. Deb, A. Pratap, S. Agarwal, T. Meyarivan, A fast and elitist multiobjective genetic algorithm: NSGA-II, IEEE Trans. Evol. Comput. 6 (2) (2002) 182–197.
[96] P. Mojaver, S. Khalilarya, A. Chitsaz, M. Assadi, Multi-objective optimization of a power generation system based SOFC using Taguchi/AHP/TOPSIS triple method, Sustain. Energy Technol. Assessments 38 (2020) 100674.
[97] X. Ye, Y. Kang, Z. Yan, B. Chen, K. Zhong, Optimization study of return vent height for an impinging jet ventilation system with exhaust/return-split configuration by TOPSIS method, Build. Environ. 177 (2020) 106858.
[98] A. Fetanat, H. Mofid, M. Mehrannia, G. Shafipour, Informing energy justice based decision-making framework for waste-to-energy technologies selection in sustainable waste management: a case of Iran, J. Clean. Prod. 228 (2019) 1377–1390.
[99] B. Shah, H. Lakhani, K. Abhishek, S. Kumari, Application of fuzzy linguistic modeling aggregated with VIKOR for optimal selection of solar power plant site: an empirical study, Renewable Energy and Climate Change: Proceedings of REC 2020 (2019) 119–127. Springer.